



SAPIENZA
UNIVERSITÀ DI ROMA

Characterization of the drift chamber's gas mixture in MEG II experiment

Facoltà di Scienze Matematiche Fisiche e Naturali

Corso di Laurea Magistrale in Physics - Fundamental Interactions: Theory
and Experiments

Candidate

Elisa Gabbrielli

ID number 2068059

Thesis Advisor

Prof. Cecilia Voena

Co-Advisor

Prof. Francesco Renga

Academic Year 2023/2024

Thesis defended on 16 December 2024
in front of a Board of Examiners composed by:

Prof. Shahram Rahatlou (chairman)

Prof. Paolo Postorino

Prof. Paolo Pani

Prof. Rinaldo Trotta

Prof. Ugo Giuseppe Aglietti

Prof. Alessandro Paiella

Prof. Oriele Palumbo

Characterization of the drift chamber's gas mixture in MEG II experiment
Master's thesis. Sapienza – University of Rome

© 2024 Elisa Gabrielli. All rights reserved

This thesis has been typeset by L^AT_EX and the Sapthesis class.

Author's email: gabrielli.2068059@studenti.uniroma1.it

Contents

Introduction	iv
1 Physics Motivation	1
1 The Standard Model	1
2 The Muon Decay	3
3 Charged Lepton Flavour Violation	5
3.1 μ cLFV decays	6
3.2 τ cLFV decays	12
2 MEG II Experiment	14
1 Signal and Background	15
1.1 Signal	15
1.2 Background	16
2 Beamline	17
3 Photon Detector	19
4 Positron Spectrometer	21
4.1 Cylindrical Drift Chamber	21
4.2 COBRA Magnet	24
4.3 Timing Counter	25
5 Radiative Decay Counter	27
6 DAQ System	28
3 A TPC to Characterize the CDCH Gas Mixture	30
1 Time Projection Chambers	31
2 Design and Simulations	33
2.1 ANSYS simulations	36
2.2 Garfield simulations	40
3 Preparation of the Measurement Setup	41

3.1	TPC Assembly	41
3.2	The UV laser	44
3.2.1	Ionization by a UV Laser	44
3.2.2	Laser Alignment	46
3.3	Preparation of the gas mixture	48
4	Measurements and Data Analysis	50
1	Experimental Procedure	51
2	Preliminary Tests	51
2.1	Flowmeter Calibration	52
2.2	Mixture stability	53
3	Data analysis	56
3.1	Drift velocity	62
3.2	Attachment coefficient	65
3.3	Garfield comparison	69
	Conclusions	72
	A Fit-parameters tables	75
	Bibliography	80

Introduction

The MEG II experiment, which is the upgrade of the MEG experiment, is placed at the Paul Scherrer Institute (PSI) in Switzerland, and has been designed to search for the charged Lepton Flavour Violation (cLFV) process $\mu^+ \rightarrow e^+\gamma$. It is a highly suppressed process in the Standard Model (SM), with a branching ratio below the feasible experimental sensitivity by several order of magnitudes, meaning that a signal would imply the existence of physics beyond the Standard Model (BSM). The photons and positrons produced in the active volume of the MEG II experiment are detected by a liquid Xenon calorimeter and a gaseous cylindrical drift chamber (CDCH), respectively. The gas mixture that fills the chamber is based on a helium-isobutane in a 90:10 ratio, with the addition of $(1 \div 2)\%$ isopropyl alcohol and 0.5% oxygen. By combining the MEG result with the data collected in the first two years of running, MEG II was able to set the most stringent upper limit on the branching ratio of the cLFV muon decay to date: $BR(\mu^+ \rightarrow e^+\gamma) < 3.1 \times 10^{-13}$ at 90% C.L.[1].

This thesis aims to characterize different variants of the gas mixture used in the MEG II drift chamber. In particular, we want to investigate helium-isobutane mixtures with a 90:10 ratio, with the addition of 2% isopropyl alcohol and different oxygen concentrations: 0%, 0.2%, 0.35% and 0.5%. These mixtures are studied under different drift fields, with intensities of 700 V/cm, 1000 V/cm, 1250 V/cm and 1500 V/cm, reflecting the typical field range within the drift cells of the MEG II drift chamber operate. Some critical properties to be measured are: drift velocity, which is the average velocity attained by electrons and ions generated by the ionization of a gas mixture when subjected to an electric field; attachment coefficient, which is the probability per unit of length that an electronegative element (like the oxygen) capture electrons, affecting the signal collected by the detector; ageing rate, which is related to the deterioration of the electrodes when collecting a large amount of ionization charge. While the ageing rate measurement will be the subject of a future, dedicated study, we are going to present the results of the attachment coefficient and drift velocity measurements conducted at the Laboratori Nazionali di Frascati (LNF)

and performed using a Time Projection Chamber (TPC). We chose a TPC rather than a drift chamber, as in the MEG II experiment, because the TPC's homogeneous electric field is better suited for studying the drift properties of a gas mixture.

In Chapter 1 we are going to introduce the Standard Model and the charged Lepton Flavour Violation processes, focusing on the muon decays, while in Chapter 2 the MEG II experiment is described in details. Finally, Chapters 3 and 4 will focus on our study, in particular, in Chapter 3 the TPC used to perform our measurements and the experimental setup are described, while Chapter 4 outlines our results.

The motivation for these measurements is related to the innovative nature of the MEG II mixture together with the scarcity of literature on similar gas mixtures (our primary reference being the work of Golovatyuk et al. (2001)[2]). In particular, the unusually high oxygen concentration of the mixture, necessary to guarantee an operational stability of the drift chamber in combination with isopropyl alcohol, also introduces a sizeable electron attachment. Since this effect cannot be accurately predicted by the existing simulation tools, direct measurements are necessary. Moreover, ageing studies have been performed on CDCH prototypes considering a pure helium-isobutane 90:10 mixture, and a 25% gain loss per year was expected in MEG II[3]. However, no evidence of gain loss has been observed during three years of operation, indicating a possible ageing retarding effect of alcohol and oxygen. These factors highlight the importance of characterizing this mixture, not only for a complete understanding of the MEG II CDCH but also as a long-term resource for gaseous detectors in future experiments that could benefit from a mixture with similar properties.

Chapter 1

Physics Motivation

The Standard Model (SM) of particle physics postulates the three fundamental interactions which are the strong, the electromagnetic and the weak interaction while it does not integrate the gravitational force.

The SM was established in the latter half of the 20th century and it has been successfully tested with a large number of experiments. Nevertheless, there are many phenomena in elementary particle physics that are not explained by the SM, for example the origin of the neutrino mass. Given that, many nowadays experiments are looking for evidences for new physics Beyond Standard Model (BSM) that can be interpreted as extension models to the SM, in order to reconstruct the complete theory. Such models have been searched in direct ways, exploiting new symmetries in colliders but also in indirect ways: one of the main method to search for BSM models is looking for charged Lepton Flavour Violation (cLFV) processes.

In this chapter we will go through some theoretical aspects of the Standard Model and some experiments regarding the cLFV, showing their results.

1 The Standard Model

The Standard Model of particle physics is based on a gauge theory with a symmetry described by the group $SU(3)_C \otimes SU(2)_L \otimes U(1)_Y$, where C is the colour charge, L is the chirality and Y is the hypercharge. Particles are grouped in two categories as shown in Figure 1.1: fermions, which are semi-integer spin particles and are the constituents of the matter, and bosons, integer spin particles referred to as the mediators of the interactions. One can also consider the anti-matter sector which implies the existence of anti-fermions.

The strong interaction is associated to $SU(3)_C$ and it is mediated by the gluon

mass →	~2.3 MeV/c ²	~1.275 GeV/c ²	~173.07 GeV/c ²	0	~126 GeV/c ²
charge →	2/3	2/3	2/3	0	0
spin →	1/2	1/2	1/2	1	0
	u up	c charm	t top	g gluon	H Higgs boson
QUARKS					
	~4.8 MeV/c ²	~95 MeV/c ²	~4.18 GeV/c ²	0	
	-1/3	-1/3	-1/3	0	
	1/2	1/2	1/2	1	
	d down	s strange	b bottom	γ photon	
	0.511 MeV/c ²	105.7 MeV/c ²	1.777 GeV/c ²	91.2 GeV/c ²	
	-1	-1	-1	0	
	1/2	1/2	1/2	1	
	e electron	μ muon	τ tau	Z Z boson	
LEPTONS					
	<2.2 eV/c ²	<0.17 MeV/c ²	<15.5 MeV/c ²	80.4 GeV/c ²	
	0	0	0	±1	
	1/2	1/2	1/2	1	
	ν_e electron neutrino	ν_μ muon neutrino	ν_τ tau neutrino	W W boson	
					GAUGE BOSONS

Figure 1.1. Elementary particles in the SM.

g , while the electroweak interaction is associated to $SU(2)_L \otimes U(1)_Y$ where Z^0 and W^\pm bosons are the mediators of the weak interaction while the γ is the mediator of the electromagnetic interactions. Fermions are divided into leptons and quarks and both of them are further divided into three generations each composed by a quark doublet and a lepton doublet. Quarks can interact through each of the three fundamental interactions and they do not exist as free particles but only as the constituents of hadrons due to the so called strong confinement. Leptons, instead, do not undergo strong interaction but exist as free particles.

Fermions' masses arise from the Yukawa lagrangian, which includes fermion fields and the Higgs field H , in the unitary gauge, where the Higgs takes the Vacuum Expectation Value (VEV):

$$\langle H \rangle = \frac{1}{\sqrt{2}} \begin{pmatrix} 0 \\ v + h(x) \end{pmatrix}$$

where h is the physical Higgs and v is the VEV.

The corresponding lagrangian terms, then, are:

$$\mathcal{L}_Y = -(y_u)_{ij} (\bar{Q}_L)_i (u_R)_j \tilde{H} - (y_d)_{ij} (\bar{Q}_L)_i (d_R)_j H - (y_e)_{ij} (\bar{L}_L)_i (e_R)_j H + h.c. \quad (1.1)$$

where i, j runs over the three fermionic families, y_f are complex 3x3 matrices and represent the couplings where $f = u, d, e$, Q_L is the doublet of left-handed (LH) quark fields, L_L is the doublet of LH lepton fields and u_R , d_R and e_R are the right-handed (RH) singlets. The conjugated Higgs field is defined as $\tilde{H} = i\sigma_2 H^*$ where σ_2 is the Pauli matrix and it guarantees the hypercharge conservation.

In the leptons' mass eigenstates basis the Yukawa lepton terms are diagonalized so no mixing between lepton generations arises at tree-level from the Yukawa terms

and the physical Higgs h interacts only with leptons of the same generation. The mixing between leptons' generations at tree-level arises only in the Flavour Changing Charged Current (FCCC) processes, mediated by the W^\pm .

We can not claim the same for the quark sector since in the quarks' mass eigenstates basis the Yukawa quark terms are not diagonalized and this introduces a mixing between generations in this sector which is quantified by the V_{CKM} matrix.

By the way, what is clear from this original formulation of the SM is that neutrinos are massless since they are not involved in \mathcal{L}_Y .

The mass terms of the W^\pm and Z^0 bosons arise from the Spontaneous Symmetry Breaking (SSB) of the electroweak symmetry, $SU(2)_L \otimes U(1)_Y$: the massless gauge bosons W_μ^a , $a = 1, 2, 3$, of $SU(2)_L$ and B_μ of $U(1)_Y$ gain masses after the SSB given by the mass terms which show a mixing of the W_μ^3 and the B_μ bosons. After their diagonalization we obtain the Z^0 massive boson field and the γ boson field which is left massless by the unbroken $U(1)_Q$ symmetry. Then, we recast the $W_\mu^{1,2}$ in the massive W^\pm bosons.

It is important to notice that, since the diagonalizations are lead by unitary transformations, the kinetic terms and the neutral current interactions are left invariant, hence the flavour is conserved.

2 The Muon Decay

The muon μ was first observed by Anderson and Neddeemeyer at Caltech in 1936 and then confirmed by Street and Stevenson[4] at Harvard in 1937 as a cosmic-rays constituent. Very soon it was possible to measure its lifetime with increasing precision on its value. This is a very important quantity since it provides the best determination of the Fermi constant, G_F , which is crucial in the formulation of the weak interaction.

The best values for the μ mass and lifetime are respectively[5]:

$$m_\mu = 105.6583755(23) \text{ MeV}$$

$$\tau_\mu = 2.1969811(22) \times 10^{-6} \text{ s}$$

The decay modes and branching ratios of the muon are listed in Table 1.1: their values were actually measured for the μ^+ but they are listed for μ^- assuming the CPT invariance. The branching ratio (BR) is defined as the ratio between the width of a specific decay mode Γ_i and the total width Γ . The main muon decay channel is

Decay mode	Branching Ratio	CL
$\mu^- \rightarrow e^- \bar{\nu}_e \nu_\mu$	$\sim 100\%$	
$\mu^- \rightarrow e^- \bar{\nu}_e \nu_\mu \gamma$	$(6.0 \pm 0.5) \times 10^{-8}$ [a]	
$\mu^- \rightarrow e^- \bar{\nu}_e \nu_\mu e^+ e^-$	$(3.4 \pm 0.4) \times 10^{-5}$	
$\mu^- \rightarrow e^- \nu_e \bar{\nu}_\mu$	$< 1.2\%$	90%
$\mu^- \rightarrow e^- \gamma$	$< 4.2 \times 10^{-13}$	90%
$\mu^- \rightarrow e^- e^- e^+$	$< 1.0 \times 10^{-12}$	90%
$\mu^- \rightarrow e^- \gamma \gamma$	$< 7.2 \times 10^{-11}$	90%

Table 1.1. Branching ratios of the muon[5]. [a] $E_\gamma > 40$ MeV , $E_e > 45$ MeV.

the so called Michel decay, $\mu^- \rightarrow e^- \nu_\mu \bar{\nu}_e$, shown in Figure 1.2, and in the SM it is described by a V-A interaction.

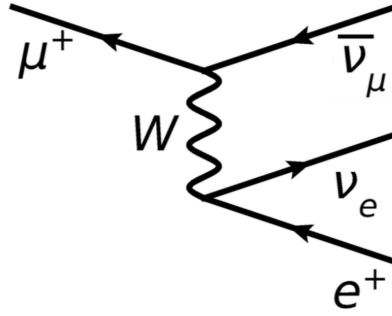


Figure 1.2. Feynman diagram of the μ^+ Michel decay.

The corresponding Hamiltonian of the Michel decay is:

$$H = -\frac{G_F}{\sqrt{2}} \bar{u}(p_{\nu_e}) \gamma^\mu (1 - \gamma^5) v(p_e) \bar{v}(p_\mu) \gamma_\mu (1 - \gamma^5) v(p_{\nu_\mu}) \quad (1.2)$$

where G_F is the Fermi constant, u and v are the Dirac spinors of, respectively, particles and anti-particles and p refers to the four-momenta. The differential decay rate of the muon decaying in its rest frame is given by:

$$d\Gamma = \frac{1}{2m_\mu} \prod_j \frac{d^3 p_j}{2E_j (2\pi)^3} \langle |M_{if}|^2 \rangle (2\pi)^4 \delta^4(p_\mu - \sum_j p_j) \quad (1.3)$$

where j is the index on the final state momenta, the δ^4 imposes the total four-momentum conservation and M_{if} is the transition matrix from the initial state $i = \mu^+$ to the final state $f = e^+, \bar{\nu}_\mu, \nu_e$, which can be evaluated as:

$$|M_{if}|^2 = |\langle e^+, \nu_e, \bar{\nu}_\mu | H | \mu^+ \rangle|^2 \quad (1.4)$$

The angular parenthesis in Equation 1.3 indicates the sum over initial and final polarizations, so:

$$\langle |M_{if}|^2 \rangle = \frac{1}{2} \sum_{pol} |M_{if}|^2$$

and then we finally write:

$$d\Gamma = \frac{1}{2m_\mu} \frac{1}{2} \sum_{pol} |M_{if}|^2 \prod_j \frac{d^3 p_j}{2E_j (2\pi)^3} (2\pi)^4 \delta^4(p_\mu - \sum_j p_j) \quad (1.5)$$

Integrating over the phase-space and assuming $m_e \ll m_\mu$, we find:

$$\Gamma(\mu^+ \rightarrow e^+ \bar{\nu}_\mu \nu_e) = \frac{G_F^2}{192\pi^3} m_\mu^5 \quad (1.6)$$

and, since $\Gamma = \frac{1}{\tau_\mu}$, by knowing τ_μ and m_μ it is possible to extract the value of G_F .

3 Charged Lepton Flavour Violation

In the SM, the lepton flavour conservation strictly relies on the fact that neutrinos are massless, since it guarantees that mass and interaction terms can be simultaneously diagonalized. By the way, it is now well established that neutrinos are massive. This has been shown by many experiments, such as Super-Kamiokande[6], SNO[7] and KamLAND[8], that measured the probability of the neutrino oscillations: a neutrino created with a specific lepton flavour number can later be measured to have a different lepton flavour number. This can be modelled by the fact that neutrinos are emitted and absorbed in weak processes as flavour eigenstates but propagate as mass eigenstates. This means that there must be a mixing between the two sets of eigenstates. The phases that describes the evolution of the flavour eigenstate in terms of mass eigenstates depend on the difference between neutrinos masses.

The experimental quantity that is measured is the probability of the transitions from one flavour eigenstate to another, $P_{\nu_\alpha \rightarrow \nu_\beta} \equiv P_{\nu_\alpha \rightarrow \nu_\beta}(\Delta m_{ij}; A)$, where Δm_{ij} is the difference between neutrino masses and A is the set of other parameters that includes the neutrino energy and the distance travelled. In conclusion, since the oscillations exist, the phases must be non-zero and so Δm_{ij} do, hence the masses themselves.

Therefore, this result is one of the clues that SM might be an approximation of some more complex model: there are many Beyond Standard Model (BSM) theories that are an extension of the SM. A powerful possible method to search for BSM signal is looking for charged Lepton Flavour Violation (cLFV) processes and this is

due to the fact that in the SM such processes have a probability that is way below the feasible experimental sensitivity given the technologies available today.

Given the experimental results, it is necessary to extend the SM introducing the neutrino mass term. However, such term can have two different theoretical motivations related to the nature of neutrinos: neutrinos are Dirac particles, so they have both RH and LH components; neutrinos are Majorana particles, they have only one chirality.

In the first case, a Dirac mass term arises from an additional Yukawa term after the electroweak spontaneous symmetry breaking (SSB) which can be build in analogy with the other fermions, in particular:

$$\mathcal{L}_D = -(y_\nu)_{ij} L_{Li} (\bar{\nu}_R)_j \tilde{H} + h.c. \quad (1.7)$$

After the SSB the neutrino mass is given by:

$$(m_\nu^D)_{ij} = \frac{v}{\sqrt{2}} (y_\nu)_{ij} \quad (1.8)$$

and by assuming tiny values for the Yukawa couplings, $Y_\nu \sim O(10^{-12})$, we can obtain a small mass compatible with the experimental results.

In the second case, instead, the Majorana mass term arises from the five-dimensional Weinberg operator defined as:

$$\mathcal{L}_M = -\frac{1}{2} m_\nu^M \bar{\nu}_L \nu_L + h.c. \quad (1.9)$$

This is an higher dimensional operator that violates the total lepton number. So far there are no evidences for the ν_R and the only way to tell if ν is a Dirac or a Majorana particle that we know is looking for the $0\nu\beta\beta$ decay, described in Figure 1.3. This diagram violates the lepton flavour number hence it is possible only if the neutrino is a Majorana particle. The CUORE[9] experiment is currently studying this process.

There are many other experiments that have searched for cLFV processes and managed to set an upper limit to their branching ratios. They mainly focus on μ cLFV decays or τ cLFV decays.

3.1 μ cLFV decays

All the available results regarding the muon channels are shown in Figure 1.4. In particular, this kind of research mainly include three channels: $\mu \rightarrow e\gamma$, $\mu \rightarrow eee$ and the $\mu N \rightarrow eN$ conversion within a Coulomb field.

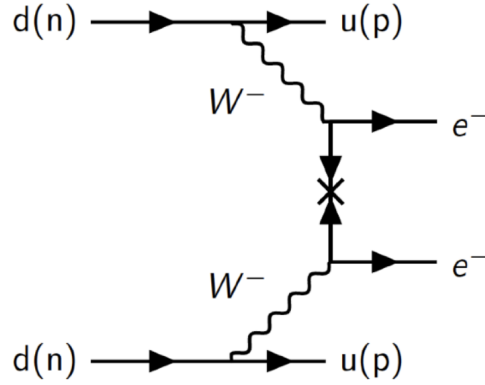


Figure 1.3. Feynman diagram of the $0\nu\beta\beta$ decay.

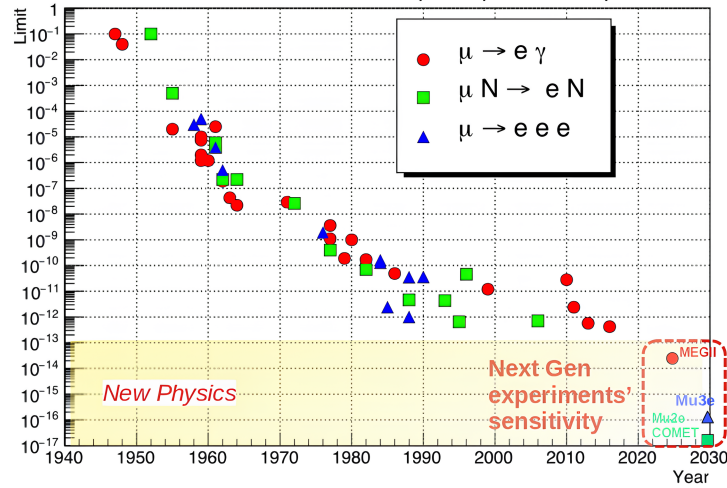


Figure 1.4. Historical progress of the cLFV search.

Thanks to the improvements in detector and beam technologies, the upper limits on the branching ratios have been continuously improved at a rate of about two orders of magnitude per decade since the first LFV experiment by Hincks and Pontecorvo[10] held in 1947.

$\mu \rightarrow e\gamma$. In the SM, this process can be described by the Feynman diagram shown in Figure 1.5.

The matrix element corresponding to the diagram is given by

$$M(\mu \rightarrow e\gamma) = i\bar{u}_e(p-q)V_\alpha u_\mu(p)\varepsilon^{*\alpha}(q) \quad (1.10)$$

where α is a Lorentz index, p and q are the four-momenta respectively of the μ and of the γ , u_μ and u_e are the Dirac spinors of the muon and the electron respectively,

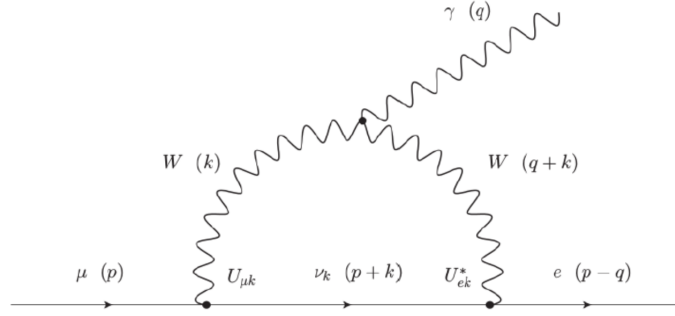


Figure 1.5. Feynman diagram of $\mu \rightarrow e\gamma$ in the SM with massive neutrinos.

ε is the polarization vector of the γ and V_α takes into account the effective μ - e - γ interaction and in terms of Lorentz invariants can be written as

$$V_\alpha = \sigma_{\alpha\beta} q^\beta (F_1 + F_2 \gamma_5) + \gamma_\alpha (F_3 + F_4 \gamma_5) + q_\alpha (F_5 + F_6 \gamma_5) \quad (1.11)$$

where $\sigma_{\alpha\beta} = \frac{i}{2}[\gamma_\alpha, \gamma_\beta]$. Using the properties of the gamma matrices and considering the limit in which $m_e \ll m_\mu$, the amplitude of the process is:

$$|M(\mu \rightarrow e\gamma)|^2 = m_\mu^4 (|A_R|^2 + |A_L|^2) \quad (1.12)$$

where $A_{R,L} = F_1 \pm F_2$ with the same dimension of a mass and they refer to right (R) and left (L) components. Since the W boson only interact with LH particles, it is necessary a chirality flip which can be due only to the mass term of the external leptons. In particular, we find that $A_R \propto m_\mu$ and $A_L \propto m_e$ and since we are in the $m_e \ll m_\mu$ limit we have $|A_L|^2 \ll |A_R|^2$ and $|A_L|^2$ is negligible, hence the decay rate expression is:

$$\Gamma(\mu \rightarrow e\gamma) = \frac{|M|^2}{16\pi m_\mu} = \frac{m_\mu^3}{16\pi} |A_R|^2 \quad (1.13)$$

Then, by computation, we obtain:

$$A_R = \frac{g^2 e}{128\pi^2} \frac{m_\mu}{M_W^4} \sum_{k=1,3} U_{\mu k} U_{ek}^* m_{\nu k}^2 \quad (1.14)$$

and using it in Equation 1.13 we can evaluate the branching ratio as:

$$BR(\mu \rightarrow e\gamma) \simeq \frac{\Gamma(\mu \rightarrow e\gamma)}{\Gamma(\mu \rightarrow e\nu\bar{\nu})} = \frac{3\alpha}{32\pi} \left| \sum_{k=1,3} \frac{U_{\mu k} U_{ek}^*}{M_W^2} \right|^2 \sim 10^{-54} \quad (1.15)$$

The numerical value of $BR(\mu \rightarrow e\gamma)$ is much smaller than the feasible sensitivity of experiments nowadays. This means that any observed signal would automatically be an evidence of new physics.

The best upper limit set so far belong to the MEG-II[1] experiment with $BR(\mu^+ \rightarrow e^+\gamma) < 3.1 \times 10^{-13}$ at 90% C.L. which has been obtained combining the final result of the MEG[11] experiment together with the data collected in the first two years of running by MEG-II. In Chapter 2 we are going to explain the experimental methodologies to search for this process.

The reason why studying cLFV processes is a very powerful strategy to look for BSM signal is illustrated in Figure 1.4 itself where it is highlighted the region of values compatible with some BSM models that predicts low but detectable branching ratios.

As an example, we can consider the SUSY-GUT model: supersymmetric models (SUSY) are extensions of the SM in which, as a result of the introduction of a new symmetry, to each particle corresponds a supersymmetric counterpart, called sparticle. In the Grand Unification Theory (GUT) approach, instead, the three coupling constants of the fundamental interactions are unified at the GUT energy scale which is of the order of 10^{16} GeV. In the SUSY-GUT model, we can write the off-diagonal terms of the slepton mass matrix as follows

$$(m_{\tilde{e}_R}^2)_{ij} = -\frac{3}{8\pi^2}(V_R)_{i3}(V_R)_{j3}^*|g_u^{33}|^2m_0^2(3 + |A_0|^2)\ln\left(\frac{M_P}{M_G}\right) \quad (1.16)$$

where V_R is the matrix that diagonalizes the lepton's Yukawa coupling, $M_P \sim 2 \cdot 10^{18}$ GeV is the reduced Planck mass, $M_G \sim 2 \cdot 10^{16}$ GeV is the GUT scale, m_0 and A_0 are respectively the universal scalar mass and coupling of the model. The possible $\mu \rightarrow e\gamma$ diagrams of this model are illustrated in Figure 1.6.

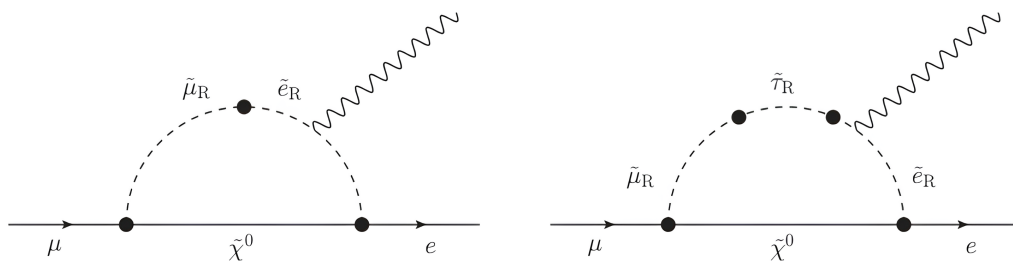


Figure 1.6. Feynman diagrams for the $\mu \rightarrow e\gamma$ decay in the SUSY-GUT model.

For different parameters of the BSM models, the decay is expected to have $BR(\mu \rightarrow e\gamma) \sim 10^{-11} \div 10^{-15}$, which is definitely measurable. By keep lowering the experimental sensitivity on the BR of this process, it is possible to downsize the phase space of the BSM parameters, setting new constraints.

$\mu \rightarrow eee$. In the SM the decay can be described by the Feynman diagram showed in Figure 1.7.

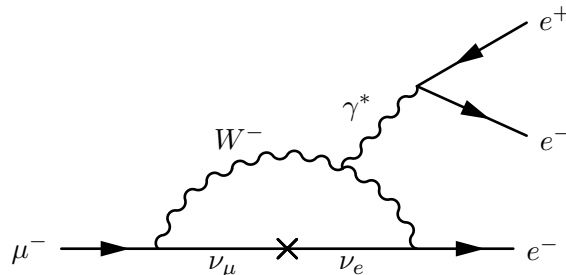


Figure 1.7. Feynman diagram of the $\mu^- \rightarrow e^- e^+ e^-$ decay in the SM.

and from a calculation analogous to Equation 1.10 one obtains[12]:

$$\frac{BR(\mu \rightarrow eee)}{BR(\mu \rightarrow e\gamma)} \sim \frac{\alpha}{3\pi} \left(\ln \left(\frac{m_\mu^2}{m_e^2} \right) - \frac{11}{4} \right) = 0.006 \quad (1.17)$$

However, if we consider supersymmetric models as extension of the SM we can introduce the diagram described in Figure 1.8 in which we obtain a branching ratio that fits in the highlighted region of Figure 1.4.

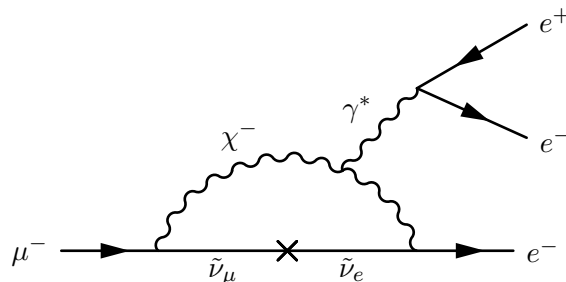


Figure 1.8. Feynman diagram of the $\mu^- \rightarrow e^- e^+ e^-$ decay in the SUSY model.

From an experimental point of view, $\mu \rightarrow eee$ is a three-body decay which can be reconstructed looking for three charged tracks that converge to one vertex. In the muon rest frame the total energy must be equal to the muon mass with a net momentum of zero. The tracker, then, must be thin so that the Coulomb scattering effects are reduced and the tracking resolution is higher. From the kinematics, we know that each particle has a momentum at most equal to $\frac{m_\mu}{2}$, the daughters particles belong to the same plane and the decay can be described by two independent variables. The energy distribution of each particle depends on the dynamics of the underlying unknown physics, so the detector must be able to reconstruct tracks with momenta ranging from few MeV up to $\frac{m_\mu}{2}$.

The main background is given by SM muon decay $\mu^+ \rightarrow e^+ \nu_e \bar{\nu}_\mu e^- e^+$, which is very difficult to discriminate when the neutrinos have a very small energy. The background associated with the internal-conversion decay should also be considered;

however, it typically produces events with lower energy and unbalanced momentum, which generally places them outside the search window.

At the moment, the best limit on the $\mu^+ \rightarrow e^+e^-e^+$ decay has been reached in 1988 by the SYNDRUM[13] experiment at PSI with a $BR(\mu^+ \rightarrow e^+e^-e^+) < 1.0 \times 10^{-12}$ at 90% C.L. The Mu3e[14] experiment, located at PSI, wants to improve the result of this channel.

$\mu^- N \rightarrow e^- N$. The muon to electron conversion is the spontaneous decay of the muon without the emission of neutrinos within a Coulomb potential of an atomic nucleus. In the Standard Model, it can be described by the Feynman diagram shown in Figure 1.9.

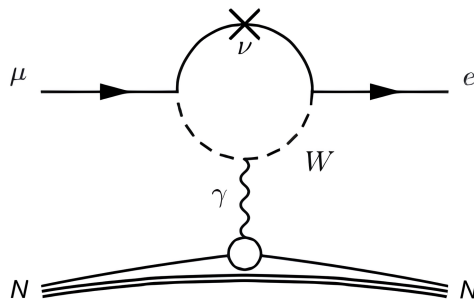


Figure 1.9. Feynman diagram of the μ -e conversion in the SM.

The contributions to this process are given by photonic (the process is mediated by photons) and non-photonic (the process is mediated by other bosons) mechanisms. The complicated expression of its branching ratio can be simplified by assuming that photonic contributions are dominant, as in some BSM models like SUSY, whose Feynman diagram is shown in Figure 1.10. Such BR depends on the nucleus taken into account and can be related to $BR(\mu \rightarrow e\gamma)$ as follows[12]:

$$\frac{BR(\mu^+ \rightarrow e^+\gamma)}{BR(\mu^- N \rightarrow e^- N)} = \frac{96\pi^3\alpha}{G_F^2 m_\mu^4} \frac{1}{3 \cdot 10^{12} B(A, Z)} \sim \frac{428}{B(A, Z)} \quad (1.18)$$

where $B(A, Z)$ represents the rate dependence on the mass number A and on the atomic number Z of the target nucleus and its numerical value is based on different approximations. Some examples are summarized in Table 1.2.

In the μ -e conversion the nucleus is unchanged, so the electron will have the same energy of the muon corrected by the binding energy and the nuclear recoil. In the previous channels we could rely on the coincidence of two or three tracks. In

Models	Al	Ti	Pb	Reference
$B_{WF}(A, Z)$	1.2	2.0	1.6	Weinberg and Feinberg (1959)
$B_S(A, Z)$	1.3	2.2	2.2	Shanker (1979)
$B_{CMK}(A, Z)$	1.1	1.8	1.25	Czarnecki, et al. (1997)

Table 1.2. Z dependence of the μ - e conversion for different approximations.

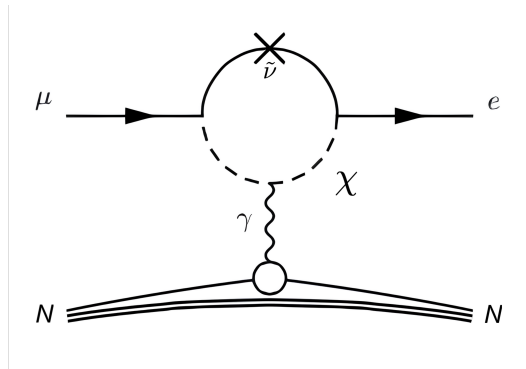


Figure 1.10. Feynman diagram of the μ - e conversion in the SUSY model.

this case, instead, we only have one charged track, so it is important to have a track reconstruction with very high resolution.

The possible source of background are: μ^- decay in orbit (DIO) which produces electrons with an energy up to the kinematic endpoint; radiative captures of π^- (RPC) which contaminate the muon beam and produce photons with an energy of the order of $m_\pi \approx 140$ MeV that convert into asymmetric e^+e^- pairs; cosmic rays that interact in the detector material and give a single electron with energy close to the endpoint; μ^- that decays in flight and produces an e^- with an energy compatible with the kinematic window.

The best limit on the $\mu \rightarrow e$ conversion process is given by the SYNDRUM II[15] experiment held at PSI in 2000, which found an upper limit on the conversion rate $R_{\mu e} < 7 \times 10^{-13}$ at 90% C.L. Two more experiments want to study this channel, Mu2e[16] at Fermilab and COMET[17] at J-PARC.

3.2 τ cLFV decays

The latest upper limits on the branching ratios are summarized in Figure 1.11, including the projection of the BELLE II[18] experiment. The τ has a lifetime $\tau_\tau \sim (290.3 \pm 0.5) \times 10^{-15}$ s, so a τ beam is more difficult to be produced, but given the large mass $m_\tau = 1776.93 \pm 0.09$ MeV it has many cLFV decay channels[5]. Some

of the main experiments that studied these channels are CLEO[19], BaBar[20] and LHCb[21].

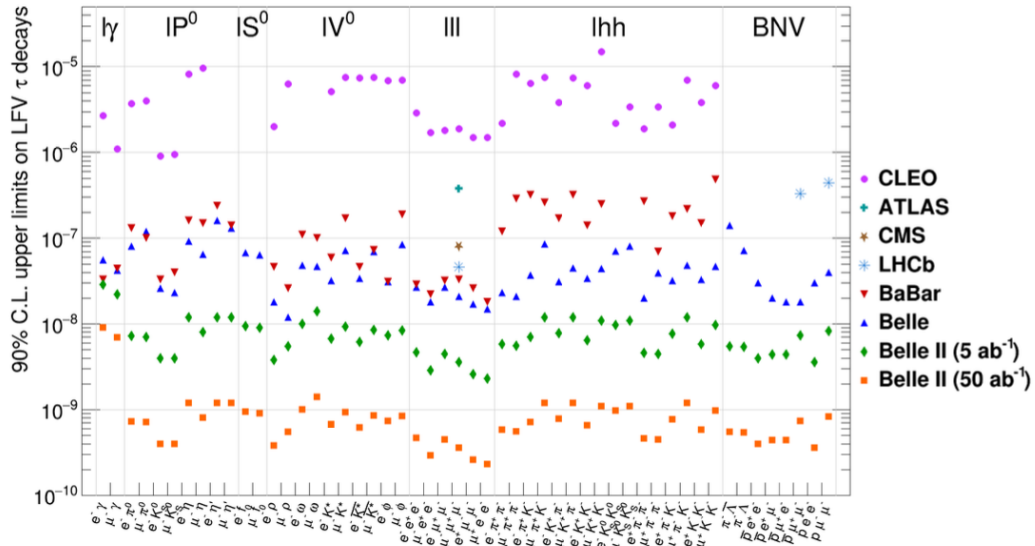


Figure 1.11. Upper limits on the τ cLFV decays[22].

Chapter 2

MEG II Experiment

The MEG experiment (Muon to Electron Gamma) was designed to search for the $\mu^+ \rightarrow e^+ \gamma$ decay and completed the data-taking in 2013 reaching a sensitivity for the branching ratio of 5.3×10^{-13} [11]. With the aim of increasing the sensitivity by an order of magnitude, reaching 6×10^{-14} , a total upgrade was needed which led to the on-going MEG II experiment started in 2019.

The MEG II experiment is located at the Paul Scherrer Institute (PSI) and it plans to continue to take data until 2026. A schematic picture of the experiment is shown in Figure 2.1.

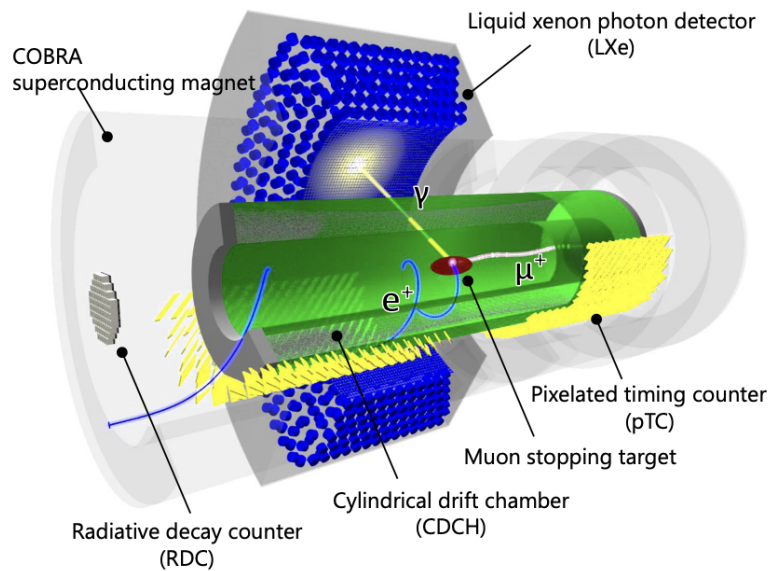


Figure 2.1. A schematic of the MEG II experiment.

Combining the data collected in the first years of running with the MEG result,

MEG II set the best upper limit so far for the $\mu \rightarrow e\gamma$ branching ratio $\text{BR}(\mu^+ \rightarrow e^+\gamma) < 3.1 \times 10^{-13}$ at 90% C.L[1].

The μ^+ beam is originated from the high-intensity proton accelerator and it is stopped on a thin plastic target, to keep a low interaction rate of the outgoing positrons. The beam intensity, ranging from $2 \cdot 10^7 \mu/s$ to $5 \cdot 10^7 \mu/s$, was optimized to keep the accidental background at a low level. Combining the photon energy E_γ , the positron momentum p_{e^+} , their relative angle $\Theta_{e^+\gamma}$ and the timing $t_{e^+\gamma}$ it is possible to distinguish the signal from the different sources of background.

The photon detector is a C-shaped calorimeter of liquid Xenon (LXe) with VUV-sensitive Multi-Pixel Photon Counters placed in the inner face. The positron spectrometer, instead, consists in three components: the central Cylindrical Drift Chamber (CDCH), to track the positrons, and the Timing Counter (TC), to measure the positron time, are surrounded by the superconductive COBRA magnet. A Radiative Decay Counter (RDC), composed by plastic scintillators and LYSO bars, is placed downstream of the CDCH with respect to the direction of the muon beam and it is necessary to distinguish the Radiative Muon Decay (RMD) background from the signal.

In this chapter, we are going to describe in details the signatures of the signal and the background of MEG II (Section 1) and the beamline characteristics (Section 2), but also all the detectors we have just mentioned (Sections 3-4-5) and the data acquisition system (DAQ) (Section 6).

1 Signal and Background

Any experiment requires a preliminary study of the signal's signature needed also to identify all possible backgrounds. This is an essential aspect for determining the appropriate detector design required to achieve the experiment's goals.

1.1 Signal

In the MEG II experiment the μ^+ are stopped in the target and decays at rest. The simple kinematic of the two-body decay $\mu^+ \rightarrow e^+\gamma$ indicates that a monochromatic photon and a monochromatic positron are emitted in opposite directions, each carrying an energy equal to half the muon mass, $E_{e^+} = E_\gamma = \frac{m_\mu}{2} = 52.83 \text{ MeV}$, and must be detected at the same time.

The number of expected signal events N_{sig} for a given branching ratio BR and

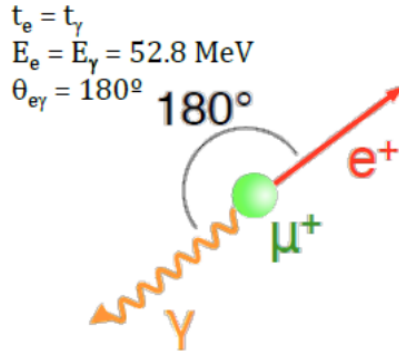


Figure 2.2. Schematic representation of the signal signature.

muon stopping rate R_μ is:

$$N_{sig} = R_\mu \times T \times \Omega \times BR \times \varepsilon_\gamma \times \varepsilon_e \times \varepsilon_s \quad (2.1)$$

where Ω is the solid angle subtended by the photon and positron detectors, ε_γ and ε_e the efficiencies of these detectors, respectively, ε_s the efficiency of the selection criteria and T the total acquisition time.

At this stage, we introduce the single event sensitivity (SES), defined as the branching ratio for which the experiment would see one single event:

$$SES = \frac{1}{N_{sig}} \quad (2.2)$$

Therefore, the lowest possible SES for an experiment that search a cLFV process is desirable in order to be sensitive to the lowest possible BR . However, increasing R_μ and T to decrease SES is not always convenient due to background events, as explained in the following section.

1.2 Background

The two main sources of background are the radiative muon decay (RMD) and the accidental coincidences of e^+ and γ signals, shown in Figure 2.3. In the RMD, $\mu^+ \rightarrow e^+ \nu_e \bar{\nu}_\mu \gamma$, the e^+ and the γ can be emitted almost back-to-back when a small fraction of the initial energy is carried by the undetected neutrinos. The discrimination of this background relies on the energy reconstruction of the e^+ and γ signals. The second type of background is the accidental coincidence of a positron from a Michel decay with a photon coming from either a RMD, Bremsstrahlung or positron annihilation-in-flight (AIF). Due to the characteristics of the background sources, to distinguish the signal from the background it is crucial to measure the

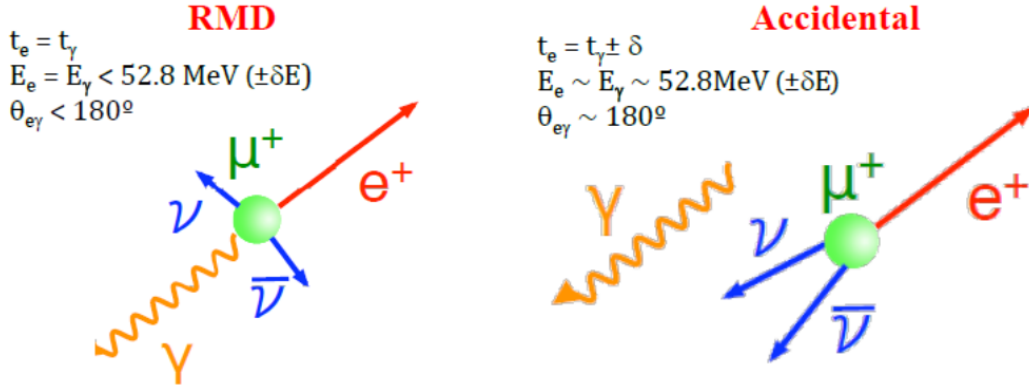


Figure 2.3. Schematic representation of the background signature.

photon energy E_γ , the positron momentum p_{e^+} , the relative angle between e^+ and γ $\Theta_{e^+\gamma}$ and their timing $t_{e^+\gamma}$ with the best possible resolution.

The number of accidental coincidences N_{acc} depends on the resolutions of the experimental quantities measured:

$$N_{acc} \propto R_\mu^2 \times \Delta E_\gamma^2 \times \Delta p_{e^+} \times \Delta \Theta_{e^+\gamma}^2 \times \Delta t_{e^+\gamma} \times T \quad (2.3)$$

where R_μ is the stopping rate of muons and T the total acquisition time. Due to the quadratic dependence on the muon stop rate, the accidental coincidences are largely dominant over the background coming from RMD when high intensity muon beams are used.

2 Beamline

The beam of μ^+ is extracted from the $\pi E5$ channel of the PSI high-intensity proton accelerator complex, as shown in Figure 2.4. The PSI Ring Cyclotron, shown in Figure 2.5, produces a 2 mA current of protons with 590 MeV of kinetic energy which travel in bunches with a repetition rate of 50.6 MHz. The proton beam hits two graphite targets where $\sim 18\%$ of the protons are stopped. The decay of π^+ , produced at rest from the interactions of protons with the targets, allows for the selection of a pure, monochromatic μ^+ with momentum $p \sim 28$ MeV. Since the π^+ lifetime of ~ 26 ns is larger than the separation between pulses, the μ^+ beam is considered continuous. The choice of a μ^+ beam over a μ^- beam is due to the higher production of π^+ compared to π^- when protons interact with the target, leading to a greater yield of μ^+ . Moreover, μ^- are more likely to be captured by atoms resulting in the emission of protons, neutrons and photons that might produce

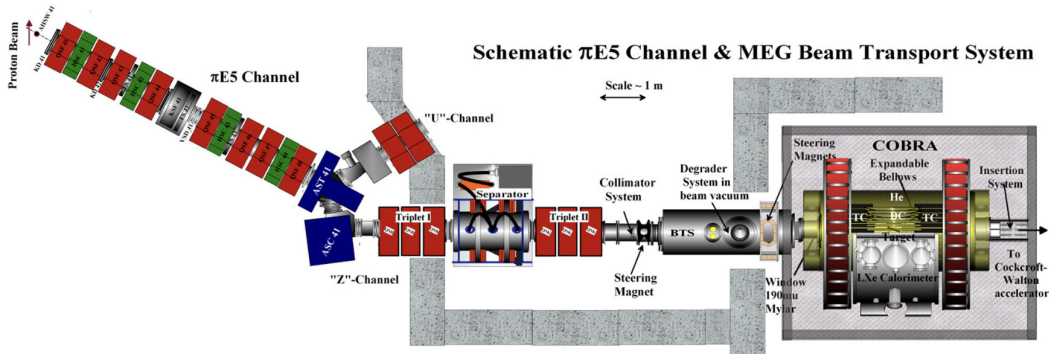


Figure 2.4. MEG II beamline with the $\pi E5$ channel and MEG II detector system incorporated in and around the COBRA magnet.



Figure 2.5. PSI Ring Cyclotron.

accidental rates in the detector. The selection of μ^+ is achieved using a Wien filter: it is based on the superposition of orthogonal electric (E) and magnetic (B) fields with intensities tuned to select only particles with the desired velocity $v = \frac{E}{B}$, while all the other particles are deflected from the main path. The Wien filter allows to discriminate per charge and mass, by combining it with a time-of-flight monitoring.

At the end of the beamline, μ^+ are stopped on the MEG II polyethylene target with 140 μm of thickness and with an angle of 15 degrees with respect to the muon beam. These characteristics have been chosen after a dedicated study to select a target with high muon stopping density, minimization of multiple scattering for the outgoing positrons, minimization of photon conversions from RMD and minimization of positron AIF or Bremsstrahlung. A very important aspect to be taken into account is the target position during the operation of the experiment since it would

introduce a systematic error in the positron trajectory reconstruction. The position is photographically monitored by a digital camera by reconstructing the pattern of printed dots on the target, as shown in Figure 3.24.

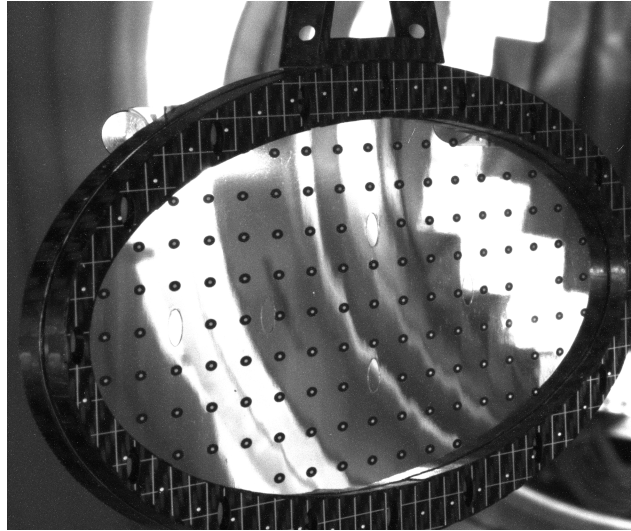


Figure 2.6. A picture of the digital camera that monitor the target positions.

To monitor the beam profile and rate, two detectors have been installed. One is the sampling scintillating fibre beam monitoring (sampling SciFi), mounted at the entrance of the vacuum beamline, in front of the spectrometer, and provides beam rate, profile measurements and particle identification in real time. It is based on scintillating fibres (SciFi) coupled to silicon photomultipliers (SiPM) and consists of a grid of two orthogonal fibre layers. The other one is a luminophore foil detector coupled with a CCD camera. It is a non-destructive beam monitoring system based on a thin CsI(Tl) scintillation foil (the luminophore) with a CCD camera system.

3 Photon Detector

The photon detector is required to provide excellent position, time and energy resolution with the purpose of minimizing the number of accidental coincidences, which are the dominant background, as explained in Section 1.2. It is a C-shaped tank, shown in Figure 2.7, with an inner radius of 67.85 cm and an outer radius of 106.35 cm, with an angular coverage of 12% of the solid angle. It is filled with 900 L of liquid Xenon (LXe) and surrounded by 846 photomultiplier tubes (PMT). A high atomic number ($Z = 54$) combined with a high density in liquid phase ($\rho_{LXe} = 2.95 \text{ g/cm}^3$), make the LXe an excellent scintillator with a radiation length $X_0 = 2.77 \text{ cm}$.

The calorimeter extends radially for 38.5 cm, corresponding to $\sim 14X_0$, meaning that it can fully contain a shower induced by a photon with energy $E_\gamma = \frac{m_\mu}{2} = 52.83$ MeV.

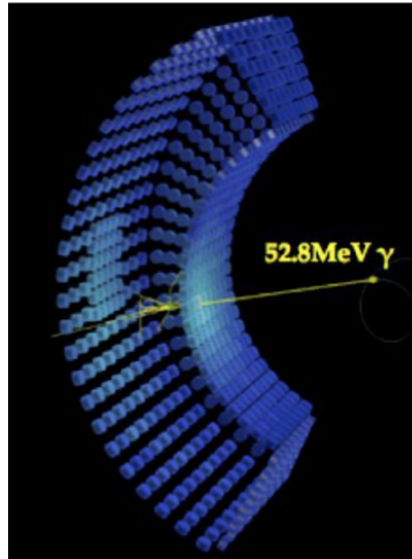


Figure 2.7. The MEG II LXe detector.

The scintillation emission, engaged by an energy deposit of at least 20 eV, features a spectrum in the Vacuum UltraViolet (VUV) range with a wavelength of $\lambda = (175 \pm 5)$ nm at an operational temperature of 165 K.

The time resolution is measured to be about 67 ps, while the energy resolution depends on the photon conversion depth: 2.7% within 8 mm from the inner face, 2% between 8 mm and 3 cm and 1.7% for deeper conversions.

The cylindrical symmetry around the stopping target implies that the photons produced by the muon decay at rest hit the calorimeter inner face perpendicularly, which is covered by solid state photon detectors of dimensions 12×12 mm² to reduce the non-uniform response that characterized the previous MEG calorimeter, as shown in the example in Figure 2.8. Since the dark count rate ($0.1\text{-}10$ MHz mm⁻¹ at room temperature, suppressed by a factor five at the LXe temperature), the sensor capacitance and the gain non-uniformity over the sensor area increase with the sensor size, the area of 12×12 mm² is formed connecting in series four smaller multi pixel photon counters (MPPC) 6×6 mm², as shown in Figure 2.9, glued on a ceramic base of 15×15 mm² which was chosen because its thermal expansion rate is similar to the one of the silicon at the LXe temperature. The sensor active area is covered with a thin high quality VUV-transparent quartz window for protection.

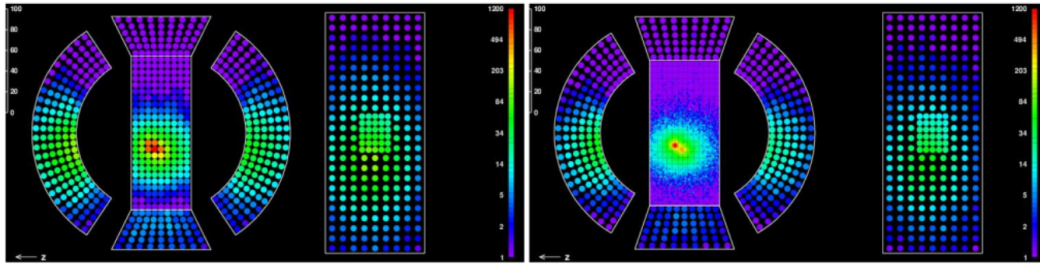


Figure 2.8. Example of scintillating light distributions detected by photo-sensors in case of (left) PMTs, as it was in MEG, and (right) smaller solid state photo-sensors $12 \times 12 \text{ mm}^2$ on the inner face for the same simulated event.

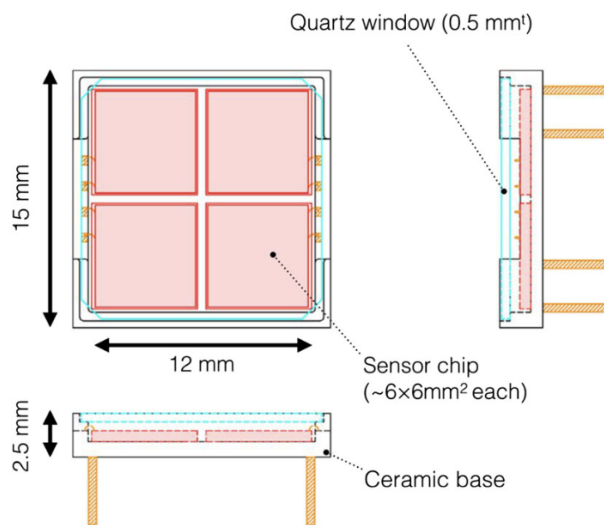


Figure 2.9. MPPC package design.

4 Positron Spectrometer

The positron spectrometer consists of the combination of a gaseous cylindrical drift chamber (CDCH) and a pixelated timing counter (pTC) both enclosed within the superconductive COBRA magnet, which provides a constant bending radius for charged particle trajectories. The CDCH, COBRA magnet, and pTC are described in detail in Sections 4.1-4.2-4.3, respectively.

4.1 Cylindrical Drift Chamber

The Cylindrical Drift Chamber (CDCH) is the main component of the positron spectrometer of the MEG II experiment since it is used to measure the positron energy, the positron angle, the production vertex in the target and, together with the

timing counter, the positron time of flight. The MEG II CDCH consists of a unique volume low-mass detector with a high granularity and a stereo wires configuration which gives a hyperbolic profile to the active volume along the beam axis (coincident with the z axis), as shown in Figure 2.10. Its mechanical structure, shown in Figure 2.11, consists of a cylinder 1.91 m long, whose axis is parallel to the beam axis, with inner radius 17 cm and outer radius 29 cm. The CDCH is placed around the beam and inside the COBRA magnet, with a cylindrical symmetry along the beam axis covering all the azimuthal angle ϕ . It has ten concentric layers azimuthally divided in twelve identical 30° sectors per layer, composed by sixteen drift cells. Each drift cell layer consists of two criss-crossing field wires planes enclosing a sense wires plane at alternating signs stereo angles (approximately ranging from 6.0° to 8.5° as radius increases) with respect to contiguous layers for a precise reconstruction of the z -longitudinal coordinate.



Figure 2.10. A picture of the entire drift chamber. The hyperbolic profile of the chamber is visible.

The elementary unit of the drift cell is approximately square, whose dimensions vary linearly depending on its position: in the innermost layer the side is 6.6 mm while in the outermost layer it is 9.0 mm. Each drift cell consists of eight cathode field wires which surround the central anode sense wires. The anode sense wires are gold-plated tungsten wires of $20\ \mu\text{m}$ diameter and are set at a positive voltage ($1500\div 1600\ \text{V}$) in order to generate the electric field in which the ionization electrons drift and are amplified. The cathode field wires are silver-plated aluminium wires of $40\text{-}50\ \mu\text{m}$ diameter connected to the ground. The configuration of the drift cells at the centre of the CDCH is shown in Figure 2.12. To equalise the gains of the innermost and outermost layers, two guard wires layers with $50\ \mu\text{m}$ silver-plated

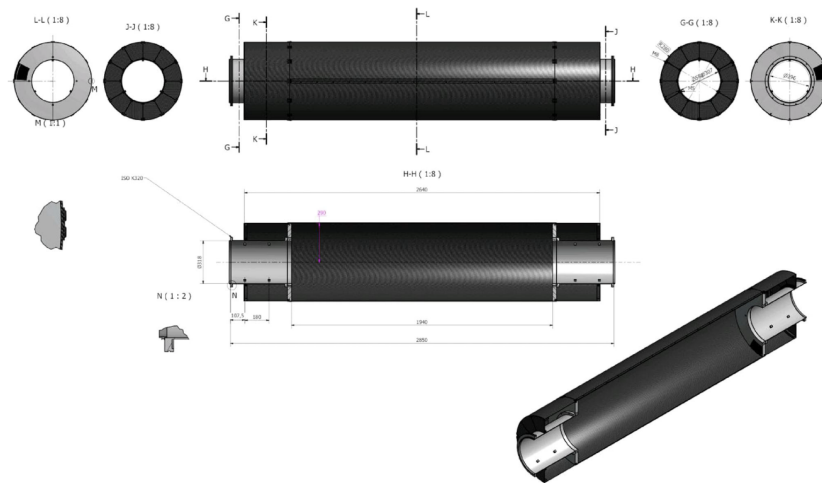


Figure 2.11. Cylindrical drift chamber structure.

aluminium have been added at proper radii and at appropriate voltages.

The CDCH is readout from both ends of each sense wire with a low noise, low distortion and wide bandwidth differential pre-amplification stage, to work as front-end (FE), followed by the waveform digitizer, the WaveDream board.

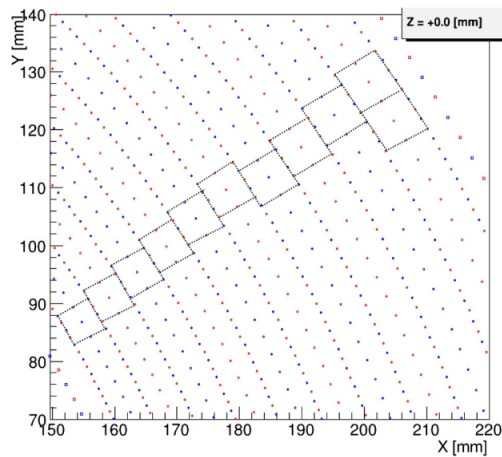


Figure 2.12. Drift cells configuration at the centre of CDCH.

A carbon fibre support structure guarantees the proper wire tension and the CDCH volume is delimited by a 2 mm thick carbon fiber shell at the outer radius and by a 20 μm aluminized mylar foil at the inner radius.

The CDCH is closed at both ends by two 30 mm thick gold-plated aluminium wheels with twelve radial spokes. On both the internal faces of the end plates there are four perforated pipes which allow the flowing of the gas inside the drift chamber

with a total volume of about 380 L. The gas used to fill the drift chamber is a helium-isobutane mixture at a 90:10 ratio with the addition of $(1 \div 2)\%$ of isopropyl alcohol and 0.5% of oxygen. The helium is very convenient in this context due to its very large radiation length $X_0^{he} \sim 5300$ m at standard temperature and pressure, implying a small contribution to the multiple scattering, but also due to its high ionization potential of 24.6 eV: with this threshold a crossing particle produces only a small number of primary electron-ion pairs in the gas mixture. A small amount of isobutane is required as a quencher to avoid self-sustained discharge. The 10% is sufficient as it raises the number of primary ionisation pairs to $\sim 13 \text{ cm}^{-1}$ though lowers the mixture radiation length to $X_0 \sim 1300$ m. Unfortunately, the use of an organic quencher also results in additional problems after exposure to high radiation fluxes. The recombination of dissociated organic molecules results in the formation of solid or liquid polymers which accumulate on the anodes and cathodes, contributing to the ageing of the chamber. The other additives were necessary to guarantee an operational stability of the experiment. With a total number of wires of 13056 the equivalent radiation length has been measured to be $1.58 \cdot 10^{-3} X_0$ when the chamber is filled with the helium-isobutane mixture in the ratio 90:10. Preliminary tests have been done on prototypes in a cosmic-ray facility and a test beam has been performed showing an expected spatial resolution of $\sim 100 \mu\text{m}$ [23]. The expected tracking efficiency is 78%, while the matching efficiency of the drift chamber with the timing counter reaches 90%.

4.2 COBRA Magnet

The COntant Bending RAdius (COBRA) magnet is a superconducting magnet, which surrounds all the detectors except for the LXe calorimeter. COBRA generates an axial graded magnetic field with a cylindrical symmetry along the z -axis. At the centre, corresponding to $z = 0$, the field reaches the maximum intensity of 1.27 T and decreases moving from the centre down to 0.49 T near the CDCH endcaps, as shown in Figure 2.13. The gradient magnetic field is specifically designed so that the positrons of same momentum emitted from the target follow a trajectory with an almost constant bending radius weakly dependent on the emission polar angle θ . Moreover, the positrons emitted at $\cos\theta \sim 0$ are quickly swept away after few turns within the spectrometer, as it is shown in Figure 2.14.

COBRA is composed by five coils with different radii: one central coil, two gradient coils and two end coils. The central coil thickness is $0.197 X_0$ to minimize the energy loss of the photons before they arrive to the LXe calorimeter.

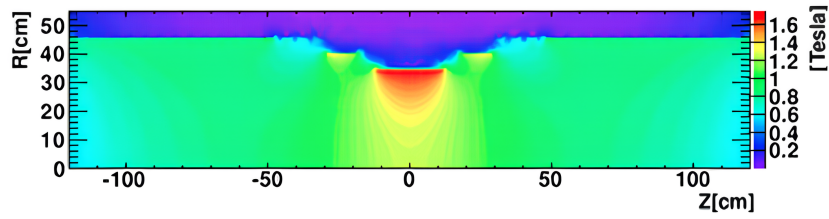


Figure 2.13. Gradient magnetic field generated by the COBRA magnet.

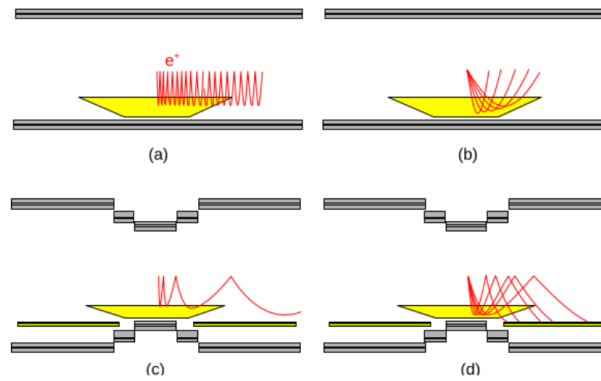


Figure 2.14. Positron tracks in the COBRA magnet field (figure (c) and (d)), compared with those in a uniform magnetic field (figure (a) and (b)). In (a) and (c) the positron is emitted perpendicular to the direction of the beam.

Normal conductive magnets are installed at both sides of COBRA in order to reduce the strength of the magnetic field in the region in which it would affect the calorimeter's electronic performances.

4.3 Timing Counter

The timing counter is used to measure the time of flight of the positron from the muon decay. The pixelated timing counter (pTC) used in the MEG II experiment, shown in Figure 2.15, is based on two semi-cylindrical super-modules, mirrored with respect to each other, with 256 $90 \times 40 \times 5$ mm³ scintillating tiles each. Each counter is a ultra-fast scintillator tile, shown in Figure 2.16, with SiPM readout. Sixteen counters form a line in the longitudinal (z) direction with a 5.5 cm interval, and sixteen lines are cylindrically arranged at a 10.3° interval, alternately staggered by half a counter. The counters are tilted at 45° to be approximately perpendicular to the signal- e^+ trajectories. The two super-modules are placed upstream and downstream with respect to the target, fitting the space between the CDCH and

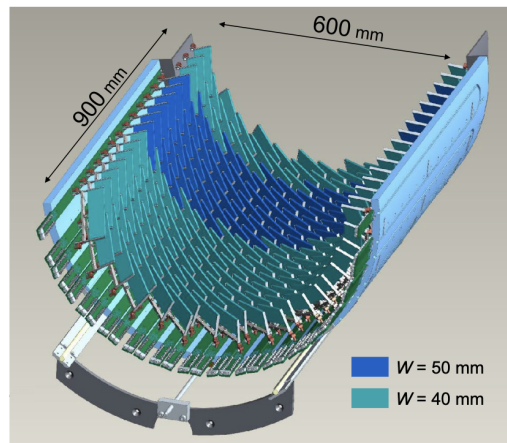


Figure 2.15. Design of the downstream pTC super-module.

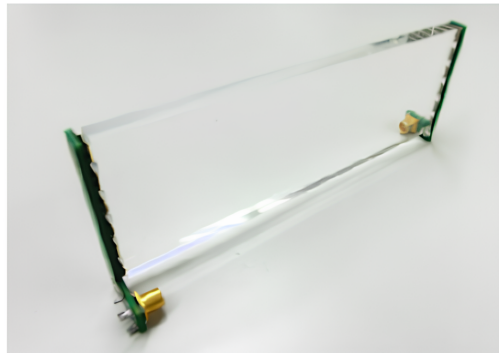


Figure 2.16. A picture of a pTC tile.

the COBRA magnet.

The pTC covers $23.0 < |z| < 116.7$ cm along the beam axis, while the angular coverage is $-165.8^\circ < \phi < 5.2^\circ$, which fully cover the angular acceptance of the e^+ from the $\mu^+ \rightarrow e^+\gamma$ decays when the photon points to the LXe photon detector.

An example of a hit pattern in the pTC by a e^+ generated by a simulated $\mu^+ \rightarrow e^+\gamma$ decay is shown in Figure 2.17, where the CDCH is not drawn. After applying the whole reconstruction analysis, the time resolution of the pTC has been estimated to reach the value of ~ 40 ps.

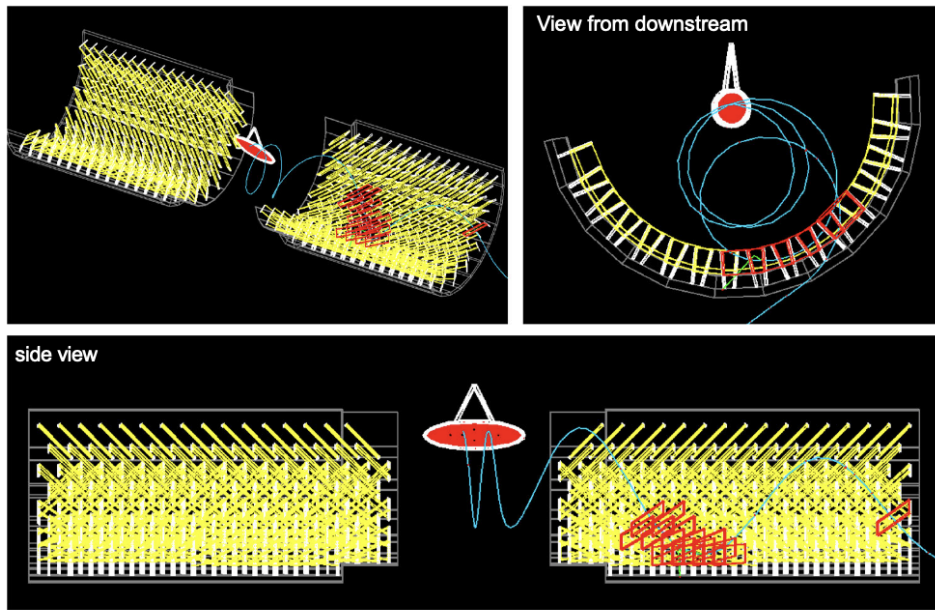


Figure 2.17. Hit pattern in the pTC of a positron from simulated $\mu^+ \rightarrow e^+\gamma$.

5 Radiative Decay Counter

The Radiative Decay Counter (RDC) is a detector dedicated to reduce the dominant accidental background in MEG II and it is installed downstream of the CDCH, as shown in Figure 2.18. As explained in Section 1.2, the photons

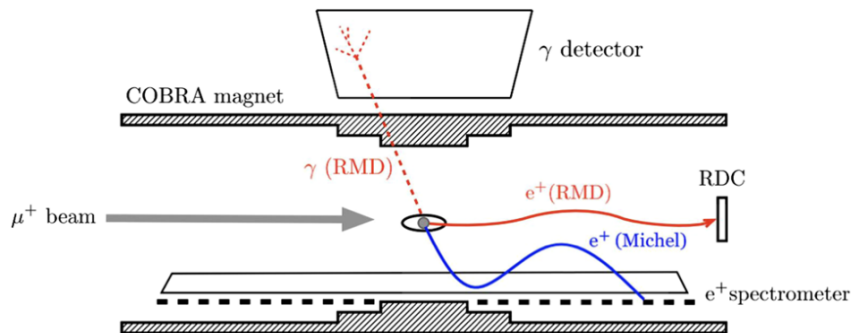


Figure 2.18. Schematic of the low-energy positron detected by the RDC

responsible for the accidental background can be produced by RMD or AIF. While the contribution of the photons from AIF can be reduced by the CDCH (see Section 4.1), the contribution from RMD photons are unaltered. In particular, the RMDs with high-energy photons produce low-energy positrons with helical trajectories around the magnetic field axis. Such low-energy positrons are not detected by

neither the pTC nor the CDCH while the high-energy photons interact with the LXe detector. The purpose of the RDC, then, is to detect RMD low-energy positrons. The time coincidence of a high-energy photon in LXe detector with a low-energy positron in the RDC allows the identification of RMD background. According to simulations, the RDC can detect $\sim 42\%$ of the RMD photon background with $E_\gamma > 48$ MeV[3].

A schematic view of the RDC is shown in Figure 2.19. The detector is composed by twelve plastic scintillator bars to measure the time of the positrons, placed in front of seventy-six $2 \times 2 \times 2$ cm³ LYSO crystals to measure the positrons energy. Due to a high background rate in the region close to the beam axis, the width of the scintillators is 1 cm in the central region and 2 cm in the outer part. Each plastic scintillator is coupled with two SiPMs at the ends of the bars, while the LYSO crystal is connected to one SiPM at the downstream side.

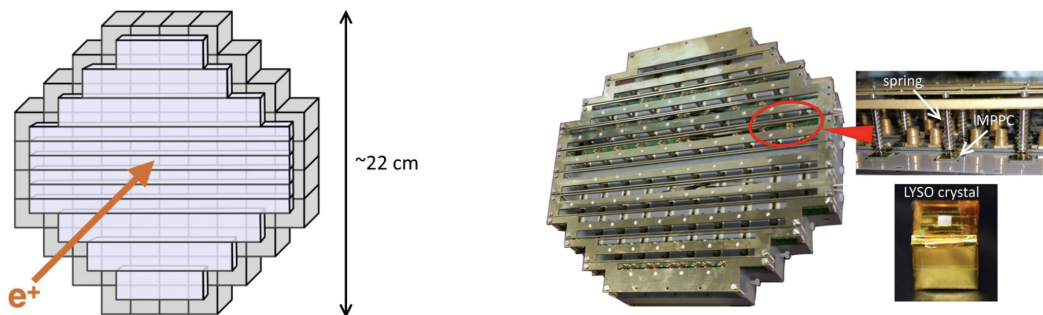


Figure 2.19. On the left a schematic of the RDC. On the right a more detailed picture.

6 DAQ System

In MEG II the total number of channels is larger than in MEG, due to the higher granularity of all subdetectors. The trigger and the DAQ system of MEG II have been integrated on a single board, the WaveDream, developed at PSI. The WaveDream board (WDB), shown in Figure 2.20, integrates the digitization, the basic trigger, DAQ functionalities, high voltage and amplification. It includes amplifiers, a waveform shaper, a bias voltage supply for the SiPM and two Domino Ring Sampler (DRS4) chips for waveform digitization, which are connected to two eight-channels analog-to-digital converters (ADC). The ADCs output are sent to a Field-Programmable Gate Array (FPGA), which perform complex trigger algorithms. The DRS4 chips sample the input signals continuously at a speed up to 5 GSPS

in an analog ring buffer. Simultaneously, a copy of the input signal is sent to the DRS4 output, where it is digitised continuously by the ADCs at 80 MSPS with a resolution of 12 bit. In case a trigger occurs, the DRS4 chip is stopped and their 1024-cell analog memory is digitised using the same ADCs that were previously used for the trigger.



Figure 2.20. A picture of the WaveDream board.

Chapter 3

A TPC to Characterize the CDCH Gas Mixture

The aim of this thesis is to characterize the gas mixture used in the drift chamber of the MEG II experiment. The mixture is based on helium-isobutane with a ratio of 90:10, with the addition of isopropyl alcohol, with a concentration varying in the range 1÷2%, and 0.5% of oxygen. This is an innovative mixture due to its unusually high oxygen concentration, which was found to be crucial to guarantee the operational stability of the detector, in combination with the isopropyl alcohol. However, the presence of the oxygen is expected to introduce also a sizeable electron attachment, reducing the size of the signals collected by the electrodes, and hence affecting the positron track reconstruction. The electron attachment is the tendency of a gas to capture free electrons and occurs in the presence of electronegative components, like oxygen. Since with our mixture, the attachment is not correctly predicted by the existing simulation tools, it must be measured experimentally. Moreover, the MEG II mixture is showing an interesting behaviour for what concerns the ageing rate, a property related to the deterioration of the electrodes when collecting a large amount of ionization charge. While with a pure helium-isobutane mixture, a 25% gain loss per year was expected when operating at a muon rate of $10^7 \mu/s$ [3], no signs of gain loss have been detected during the years of operation of the MEG II experiment with the described gas mixture. These peculiar properties make this study worth to be performed, not only for a better understanding of the MEG II CDCH, but also for future experiments that might be interested in a mixture with such characteristics, as for instance those operating at a future e^+e^- circular collider.

To achieve our purpose, a Time Projection Chamber (TPC) was designed, assembled and tested. We chose a TPC rather than a drift chamber, as in the MEG II experiment, because the TPC's homogeneous electric field is better suited for studying the drift properties of a gas mixture. In Section 1 we introduce the concept of a TPC with all its main characteristics, focusing on the features that interest us the most.

In Section 2 we will go through the simulations results of the electric field inside the TPC, that have been performed using `Garfield++`¹, a software specifically designed for the simulation of gaseous detectors, and the ANSYS 3D Maxwell module, which is a Finite Element Analysis (FEA) software.

With the setup described in Section 3, we aim to measure some of the properties of the electron drift in the gas mixture, including the attachment coefficient, while the ageing rate will be the topic of a future, dedicated study. The measurements will be performed by ionizing the gas at a specific locations inside the TPC using a pulsed UV laser.

1 Time Projection Chambers

A Time Projection Chamber (TPC) is a particle detector which was first proposed by David R. Nygren at the Lawrence Berkeley National Laboratory in 1974. It is based on the combination of electric and magnetic fields together with a sensitive volume of gas (or liquid) to perform a three-dimensional reconstruction of a particle trajectory or interaction. As shown in Figure 3.1, a charged particle passing through the gas ionizes the gas molecules, creating free electrons and positive ions along its path. The presence of an electric field, also called drift field, causes such electrons and ions to drift along the field lines toward the anode and the cathode, respectively. The cathode and anode electrodes define the drift region and consist of either wires or solid planes. The tensions supplied to the electrodes and their distance determine the intensity of the drift field. TPCs are often used within a magnetic field, parallel to the electric field, which allows to measure the momentum of the ionizing charged particles, by curving their trajectories. The magnetic field also reduces the diffusion that the electrons undergo during the drift, improving the position resolution.

When the electrons reach the anode, they enter a thin region with an intense electric field generated by wires, or other electrode patterns, where an electron avalanche is produced. The avalanche induces a signal proportional to its total

¹<https://www.google.com/url?q=https://garfield.web.cern.ch/garfield/>

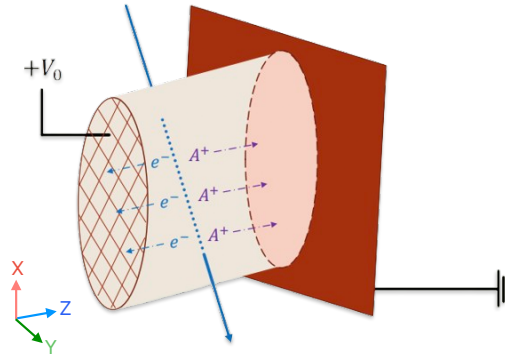


Figure 3.1. Schematic representation of the ionization inside a TPC.

charge in a readout plane which consists of pads, strips, or wires. Referring to the axis in Figure 3.1, the position of the readout component that collects the signal gives information on the XY position, while from the drift time, knowing the drift velocity, it is possible to extract the Z coordinate. Combining these informations it is possible to reconstruct the trajectory of the ionizing particle in three dimensions.

The drift velocity is related to the electric field, through the definition of the particle mobility:

$$v_{drift} = \mu E \quad (3.1)$$

where v_{drift} is the drift velocity, μ is the particle mobility and E is the electric field. The particle mobility is a particle specific property, so it has different values for electrons and ions. It is also affected by the medium characteristics (meaning that it depends on the mixture), the temperature, the pressure and the electric field intensity. In TPCs, the ionization electrons are typically assumed to move with a constant velocity, meaning that both the mixture and the electric field must be homogeneous in the drift region.

To ensure the electric field homogeneity along the drift region, an additional component is often introduced, called field cage. The field cage, shown in Figures 3.2-3.3, when present, surrounds the drift region, confining the electric field. It consists of conducting strips, or rings, connected by a series of resistors which divide the voltage uniformly between the cathode and the anode. This ensures a linear voltage gradient along the drift region. The electrodes are mounted on an insulating material to insulate them from each other and the surroundings. In this way, it is possible to guarantee a predictable and controlled drift of the particles toward the detector readout plane, where the signal is collected.

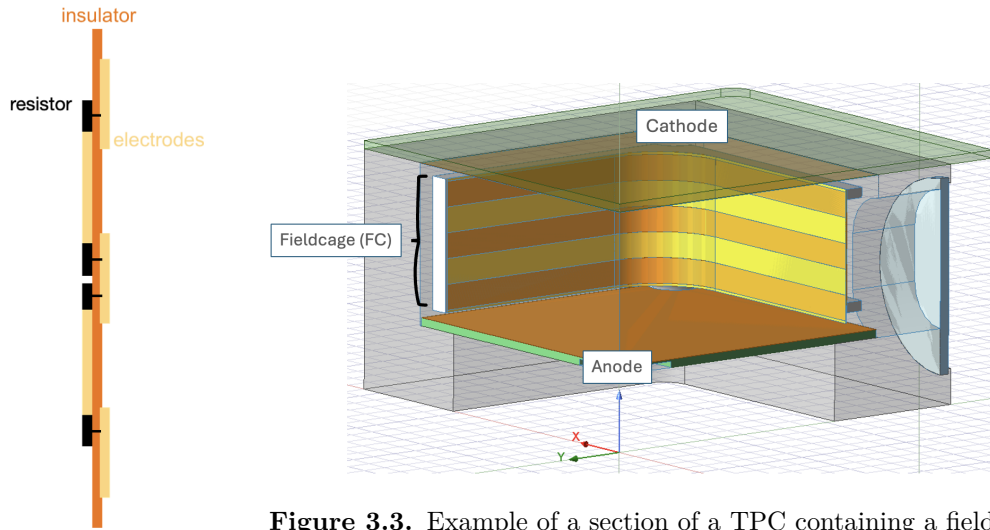


Figure 3.3. Example of a section of a TPC containing a field cage.

Figure 3.2. Schematic representation of a field cage.

2 Design and Simulations

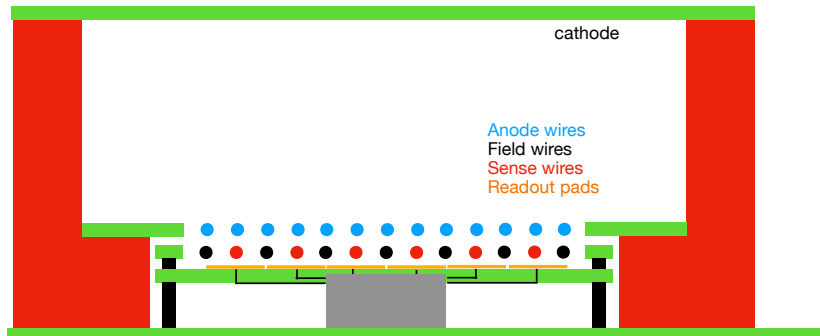


Figure 3.4. Schematic representation of the TPC (not in scale).

The TPC that we used is a $16 \times 16 \times 5 \text{ cm}^3$ plexiglass chamber, with a 3 cm drift region defined by a cathode plane, made of a copper layer on a printed-circuit board (PCB), and a plane of anode wires, as represented in Figure 3.4. This plane is obtained by soldering metallic wires on a gold-plated PCB frame (anode board). A second layer of wires, also soldered on a PCB frame (sense board), placed 0.4 cm below the anode electrode, is the amplification stage, consisting of wires with alternating voltages (sense wires at high positive voltage and field wires at ground). The sense wires are made of gold-plated tungsten with $25 \mu\text{m}$ diameter and 8.4 cm

long while the anode and the field wires are made of gold-plated aluminium with 80 μm diameter and 8.4 cm long.

The readout plane is placed 0.4 cm below the amplification stage and consists of a gold-plated layer on a PCB, with the central part subdivided in twenty-four 0.4×0.8 cm^2 pads organized in three rows centred with respect to the readout plane, as shown in Figure 3.5. The signal collected by the pads is then amplified by the front-end (FE) boards of the MEG II CDCH[3] and readout by a 16-channel WaveDream digitizer at 700 MSPS[3]. One FE board has eight channels, so we can connect two boards to the WaveDream. Actually, we observed a severe deterioration of the noise when installing more than one FE board, so we used only one of them, meaning that we could read the signal collected by only eight pads. The relation between the readout pads and the WaveDream channel is shown in Figure 3.5.

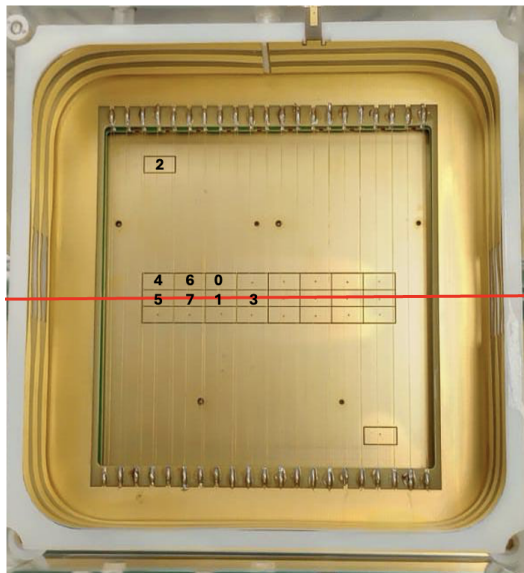


Figure 3.5. A picture of the inside of the TPC: we can see the wires and the read-out pads. The numbers identify the relation between the WaveDream channels and the pads position, while the red line represents the laser beam. Channel 2 is a reference channel and it is used for the subtraction of the common noise.

Since our detector has a small thickness-to-surface aspect ratio, a good uniformity of the drift field can be achieved without a filed cage. However, we wanted to test this hypothesis performing simulations of the electric field.

The chamber has two quartz-glass windows 3 cm wide and 2 mm thick, glued and sealed with an epoxy adhesive, which are required to let the UV laser beam enter the gas volume. Moreover, due to space optimization, the cathode and anode voltages

are both supplied from the cathode PCB. This is achieved through an insulated metallic rod, shown in Figure 3.6, connecting a dedicated pad in the cathode PCB (insulated from the copper layer) to the gold-plated surface of the anode PCB. The presence of the rod can compromise the homogeneity of the electric field. This is another effect to be studied with electric field simulations. A detailed model of the TPC is shown in Figure 3.6.

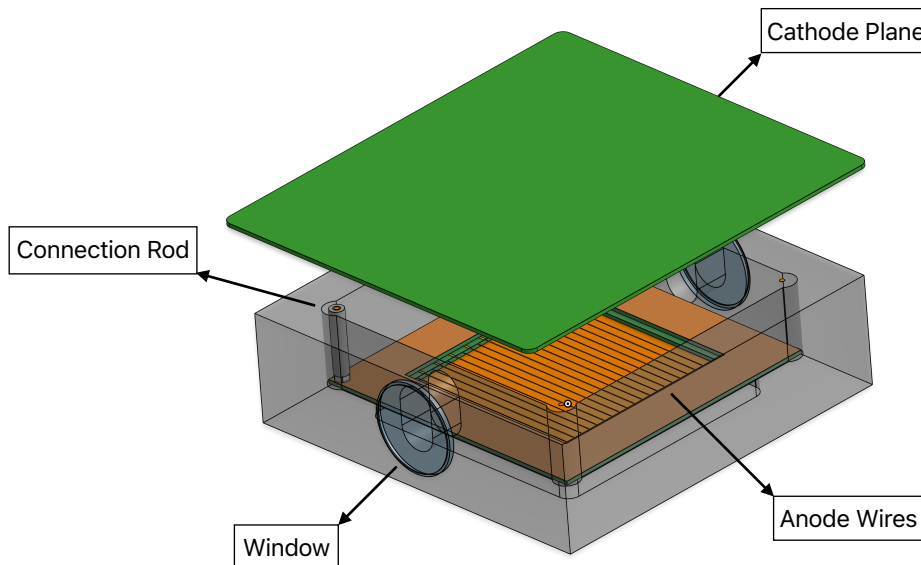


Figure 3.6. A detailed model of the TPC in which we can see the insulated connection rod and the two quartz-glass windows.

We adopt a voltage configuration with the cathode at high negative voltage, anode wires, field wires and readout plane at ground (0 V) and sense wires at high positive voltage. In this way, by setting the tension of the cathode, we can adjust the drift field. For example, assuming a good homogeneity inside the volume, if we want a drift field of intensity E in a drift region $d = 3$ cm long, the tension of the cathode must be simply set to $V_C = -dE$. The voltage of the sense wires allows to regulate the amplification gain, with a typical working point of 1350 V. For our application, we are going to explore a range of different electric field intensities without a magnetic field. In particular, we will focus on drift field of 700 V/cm, 1000 V/cm, 1250 V/cm and 1500 V/cm, which is a representative range for the field in the cells of the MEG II drift chamber.

2.1 ANSYS simulations

The homogeneity of the drift field in the chamber was investigated with simulations performed with the Maxwell 3D module of ANSYS, which takes into account all the relevant components of the detector. We also aim to identify any critical points where the electric field strength exceeds the threshold of 20 kV/cm, which is a safety value for the electric field intensity to prevent discharges in helium-based mixtures[24]. Due to computing power limits, we needed to simplify the detector model, by replacing the anode wires with a conductive plane, as shown in Figure 3.7. The effect of the wires have been separately tested with **Garfield++** (see Section 2.2). By defining each component in the ANSYS simulation and specifying materials

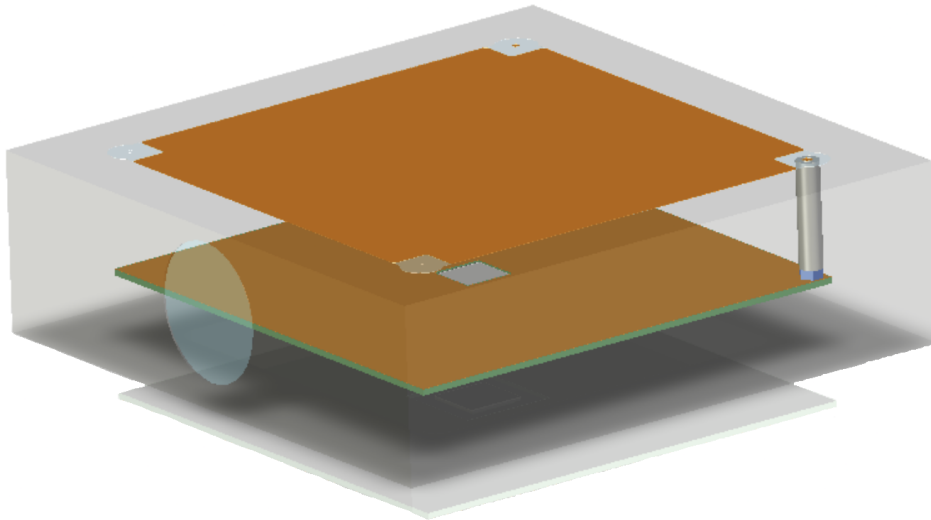


Figure 3.7. Alternative model used to test the electric field with ANSYS in which the anode wires have been replaced by an anode plane.

and voltage supplies, we could reproduce our TPC.

For our purposes, we want to produce the electric field maps in some critical regions, specifically above the readout pads, around the connection rod and near the corners of the gas volume. Starting with a nominal electric field of 700 V/cm, we checked the field along the diagonal plane that runs from the connection rod to the opposite corner, as shown in Figure 3.8. The results are shown in Figure 3.9 where it is clear that the inhomogeneity given by the rod and other structural elements does not affect the central region, where the readout is made. Moreover, the maximum value of the electric field is way below the concerning level of 20 kV/cm, where discharges might occur.

We checked also the electric field along the planes parallel to the walls passing

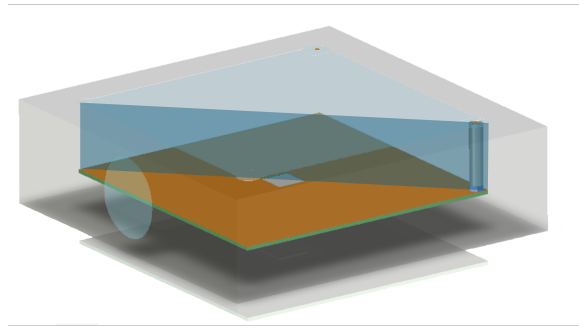


Figure 3.8. In blue the diagonal plane along which the electric field was simulated.

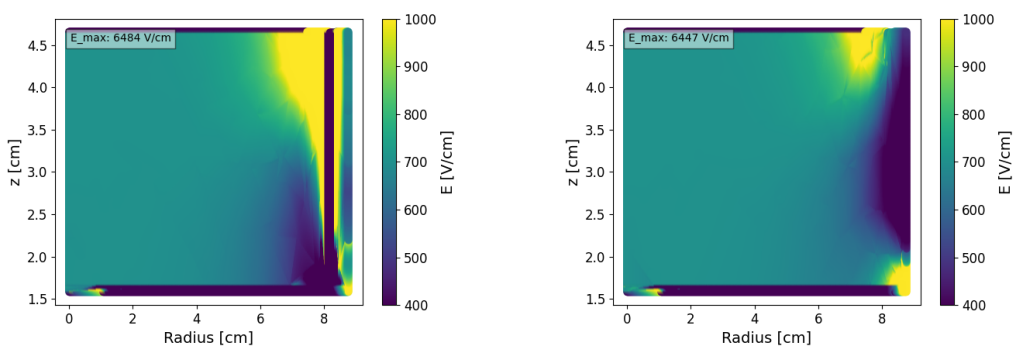


Figure 3.9. Electric field along the diagonal plane running from the connection rod to the opposite corner, with a nominal value of 700 V/cm. On the left the section from the centre to the rod. On the right the plane running along the opposite direction.

through the centre of the chamber, exploiting the symmetry of the TPC. With the YZ plane we refer to the plane that goes from the centre of the chamber and reaches the window, as shown in Figure 3.10. The XZ plane, instead, is the perpendicular one passing through the centre, as shown in Figure 3.11. Both planes considered are positioned on the connection rod side, since we want to monitor its effects. Results are shown in Figure 3.12, and similarly to before, we can conclude that the electric field is homogeneous in the readout region.

We repeated the same analysis but considering a nominal electric field of 1500 V/cm. Results are shown in Figure 3.13 where the maximum value for the electric field along the diagonal plane is of the order of the critical limit.

Changing the scale for the electric field, we can see that very high values are located in a very small region where the rod is connected to the cathode PCB, as shown in Figure 3.14. To avoid discharges, a drop of insulating glue was added around this connection point during the assembly of the detector.

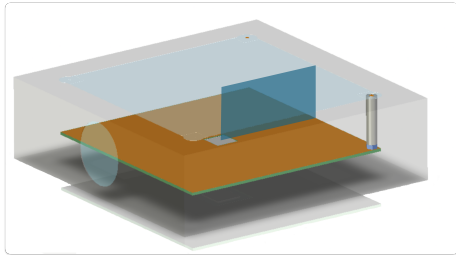


Figure 3.10. In blue the YZ plane along which the electric field was simulated.

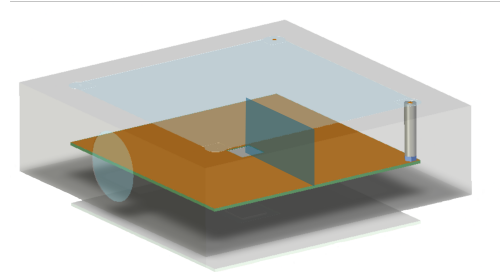


Figure 3.11. In blue the XZ plane along which the electric field was simulated.

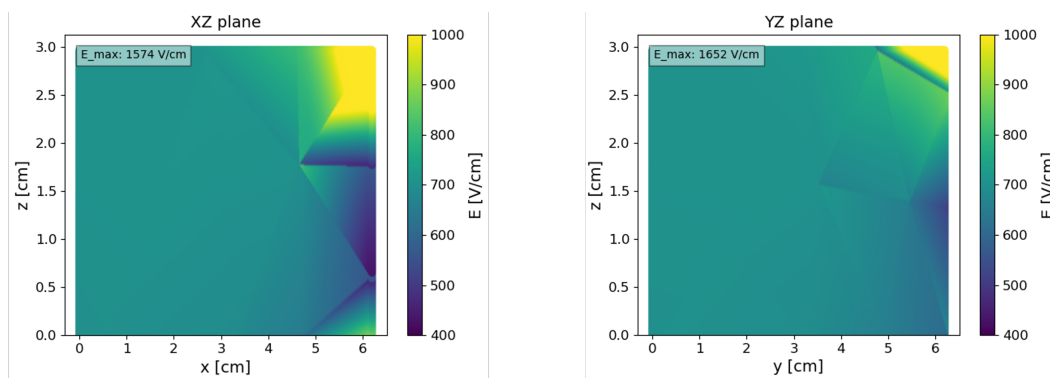


Figure 3.12. Electric field along the XZ plane (on the left) and the YZ plane (on the right) considering a nominal electric field of 700 V/cm.

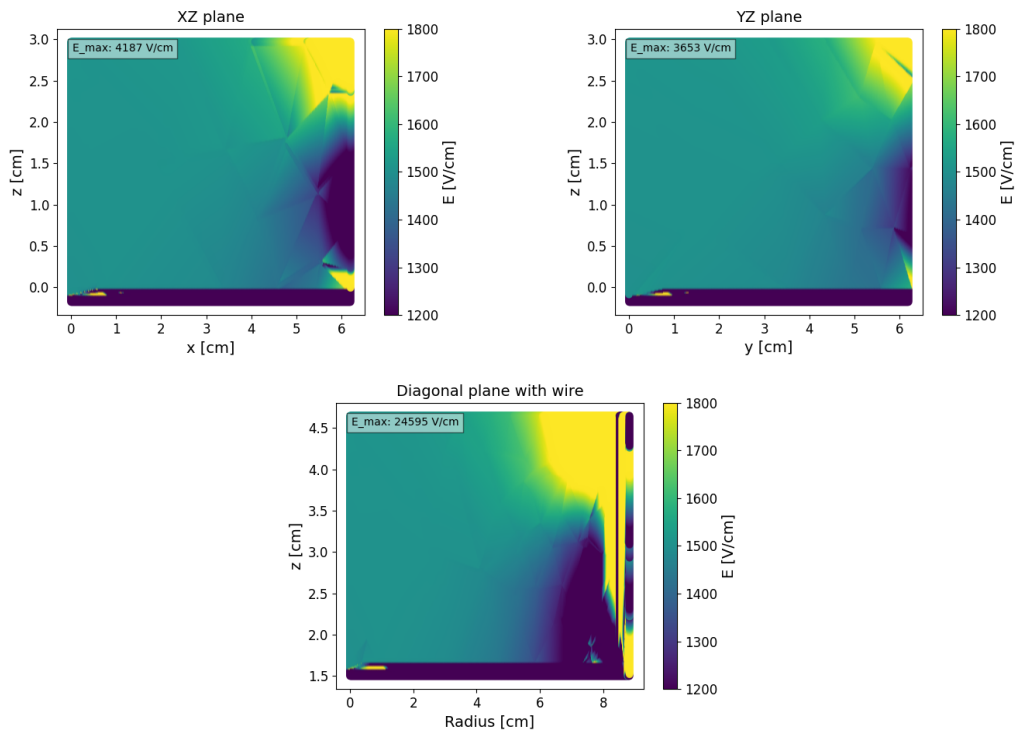


Figure 3.13. Study of the electric field along different planes with nominal value of 1500 V/cm. In the first row the electric field simulated along the XZ plane and along the YZ plane. In the second row the electric field simulated along the diagonal plane from the connection rod to the centre of the volume.

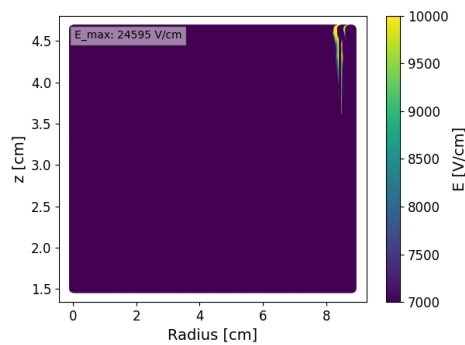


Figure 3.14. A detail of the high electric field region in the vicinity of the rod in the case of a nominal electric field of 1500 V/cm.

2.2 Garfield simulations

In ANSYS, due to computing power limits, we neglected the fact that our TPC actually has an amplification stage and an anode electrode that both consist of wires. In order to study their impact on the field homogeneity, we considered a simplified geometry shown in Figure 3.15 and we simulated the electric field using `Garfield++`. The geometry, based on the design represented in Figure 3.4, has a cathodic plane at 3 cm distance from the first layer of anode wires which in turn is placed at 0.4 cm distance from the second layer of alternating field and sense wires. Below them the readout plane at 0.4 cm distance.

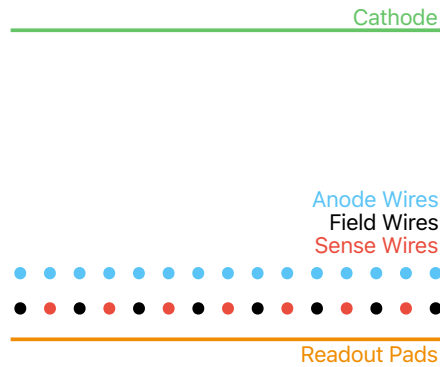


Figure 3.15. Simplified TPC model to simulate the electric field in `Garfield++`.

Once the geometry is set, it is necessary to set the voltages of each component in order to generate the electric field. We want to understand how the electric field in the readout region is affected by the presence of the two wire layers. So we simulated the electric field along the vertical lines passing through the centre of each pad. To avoid redundancy, in Figure 3.16 we show the results at different nominal electric field for only one pad. The results are consistent with the homogeneity found in Section 2.1 and the drift field is not significantly affected by the wires.

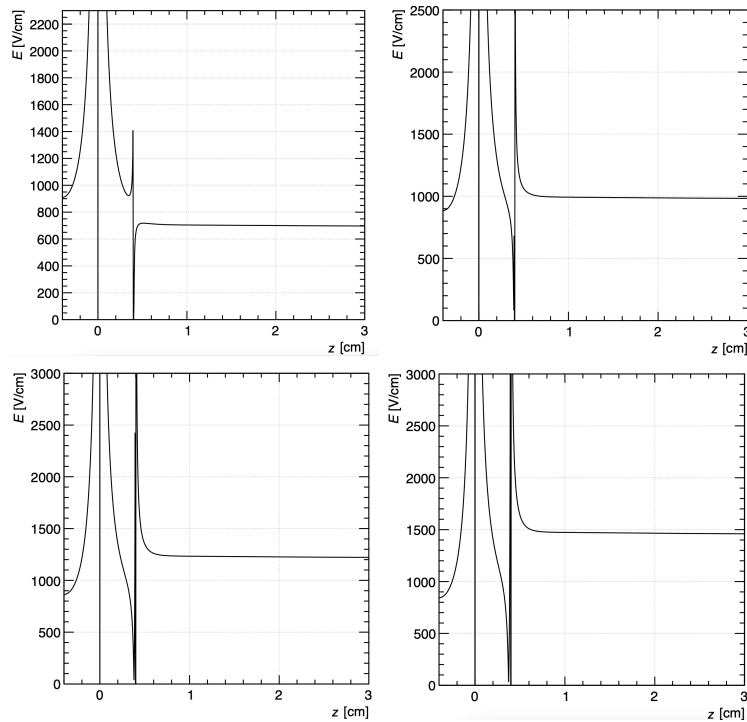


Figure 3.16. Garfield++ electric field simulations at different nominal values in the drift region along the direction that passes through the centre of one pad. From left to right, from top to bottom we have 700 V/cm, 1000 V/cm, 1250 V/cm and 1500 V/cm. The vertical lines in $z = 0$ cm and in $z = 0.4$ cm correspond to the sense wire and the anode wire positions, respectively.

3 Preparation of the Measurement Setup

Given the positive results of the simulations, we could move forward and assemble the TPC according to the design described in Section 2. The assembly procedure is detailed in Section 3.1. In Section 3.2, instead, we will delve deeper in the details of the UV laser used to illuminate the TPC for our measurements. Finally, in Section 3.3 we are going to explain in details the gas system we used in our experimental setup.

3.1 TPC Assembly

The wiring of the sense board and the anode board was carried out following few steps. First, the board was placed on a custom holder that could be horizontally adjusted to position the wire correctly, as shown in Figure 3.17. Each wire passed through a cotton cloth soaked in alcohol to remove any dirt and was secured by

two holders placed at the ends of the board. Finally, the wire was soldered onto the boards while being kept under tension using a weight of 20 g. Given the short length of the wires, the described procedure was accurate enough to prevent sagitta or electrostatic instabilities effects. The result is shown in Figure 3.18.

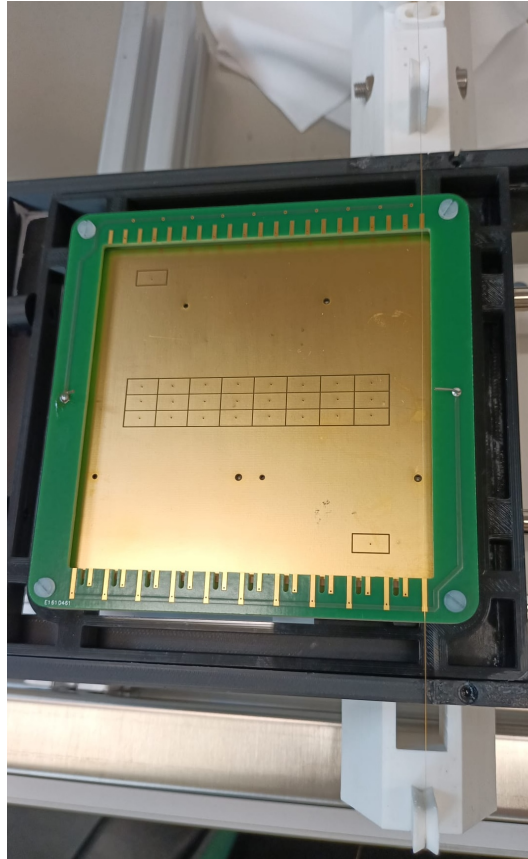


Figure 3.17. A picture taken during the wiring of one of the board.

Once the wiring was completed, we proceeded to assemble the TPC. Starting with the plexiglass chamber, whose model is shown in Figure 3.19, we had to place inside of it, from bottom to top, the pad board, the sense board, the anode board and the cathode board, as shown in Figure 3.20. At each level, the 0.4 cm space between components is set by four plastic bolt placed at the four corners and everything is held in place by four thin plastic screws. As previously explained in Section 2, an insulated connection rod was screwed into one of the corners. A spring-loaded pin, mounted on the cathode PCB, provides a good electric contact with the connection rod.

Finally, the chamber was closed by screwing the cathode board and the pad board directly onto it. O-rings sitting on dedicated grooves between the boards and

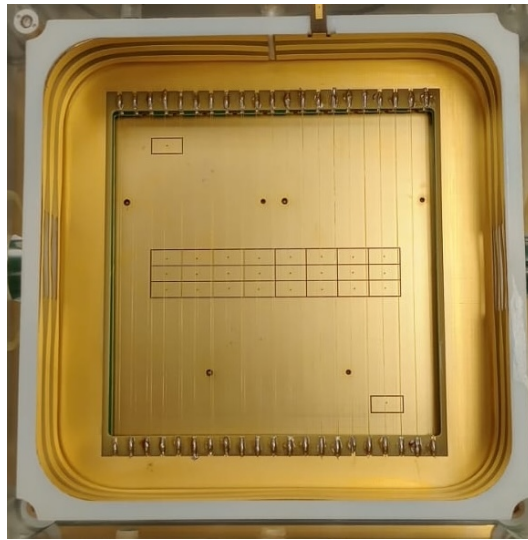


Figure 3.18. A picture of the TPC after the wiring without the cathode plane.

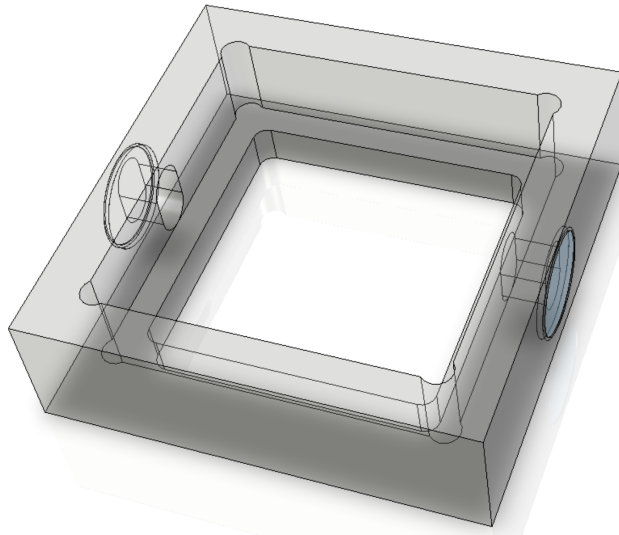


Figure 3.19. A model of the plexiglass chamber with the two windows already mounted.

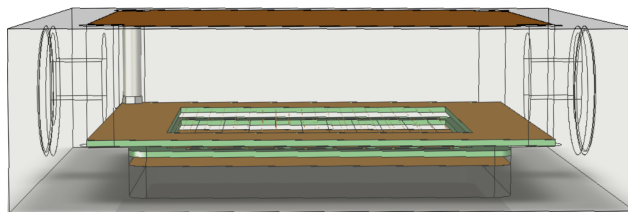


Figure 3.20. A detail of the ordering of the components inside the plexiglass chamber.
From the bottom: the pad board, the sense board, the anode board and the cathode board.

the chamber ensure the gas tightness of the assembly. The final result, including the HV and the ground connections, is shown in Figure 3.21.

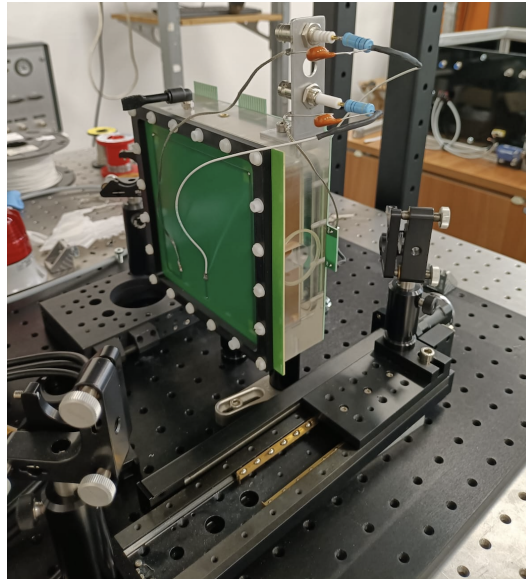


Figure 3.21. A picture of the TPC and its connections. On the side we can see also the motorized stage very important for both alignment and measurements procedures.

3.2 The UV laser

To perform our measurements, we used a pulsed UV laser to illuminate the TPC. The laser² is a Q-switched system operating at a wavelength of 355 nm, with a beam diameter of 1 mm. Its pulses have a width of 4 ns and can deliver up to 100 μJ of energy, depending on the current that can be adjusted by the user.

A Faraday cage built around the TPC and enclosing the laser path, as shown in Figure 3.22, ensures both electromagnetic shielding and operator's protection. In Section 3.2.1 we will discuss the UV laser ionization mechanism, explaining the reasoning behind the choice of this laser, while in Section 3.2.2 we will go through the procedure adopted to align the beam to the chamber.

3.2.1 Ionization by a UV Laser

The ionization of a gas mixture by a UV laser is a process known as photoionization, where the photons of the UV laser provides an energy high enough to overcome the ionization energy of the gas, resulting in the ejection of electrons and creation of

²<https://www.gophotonics.com/products/lasers/elforlight-ltd/29-23-fqs-100-1-y-355>

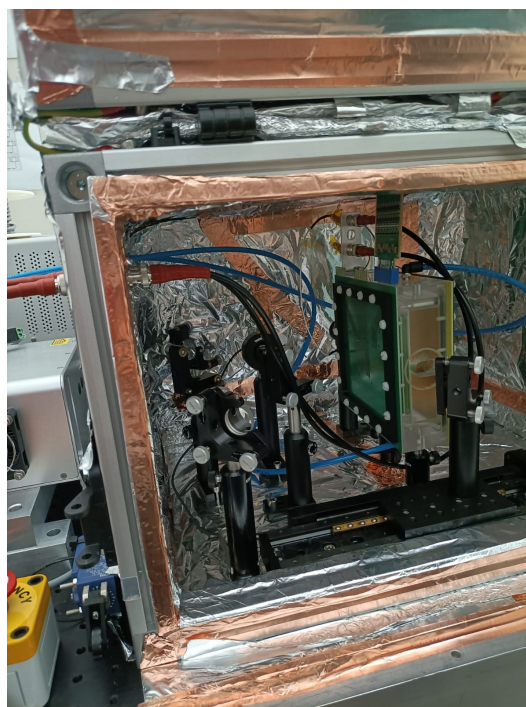


Figure 3.22. Picture of the inside of the Faraday cage with the TPC connected to the FE and the optic components. The blue pipes let the gas mixture flows through the TPC.

ions. However, if the photon energy is below the ionization threshold, multi-photon ionization (MPI) can occur, where a gas molecule absorbs two or more photons, enabling ionization. While single-photon ionization is linear with the laser intensity, MPI is a non-linear process that becomes more significant at high laser intensities, compensating for its lower probability.

Compared to other types of lasers, UV lasers are particularly effective for ionization because their photon energies are higher. Optical lasers, for example, with photon energies in the visible or near-infrared range, generally lack the energy required to ionize gases.

Moreover, a pulsed UV laser, as opposed to continuous-wave one, delivers high peak power in very short interval of time, increasing the efficiency of the MPI, even for molecules with higher ionization thresholds. The short duration of the pulses creates a localized intense ionization event, which is very convenient for our application. Using a signal generator, we could set an external trigger pulsed shaped with 20 Hz frequency to start both the laser emission and the WaveDream acquisition. Actually, the trigger pulse sent to the WaveDream was delayed by 2.1 μs with respect to the laser emission trigger in order to synchronize the WaveDream

acquisition with the collected signal.

3.2.2 Laser Alignment

To perform correctly our measurements, the laser must be aligned with respect to the TPC. So we set an appropriate system of mirrors and lenses that fits our geometry, to take the laser beam from the source to the TPC, as shown in the scheme reported in Figure 3.23. Notice that Mirror 5 is mounted on a motorized translation stage that was crucial for both the alignment and measurement procedures. The stage has a micrometric resolution and was controlled remotely through a dedicated application on a computer. To simplify the alignment procedure, we introduced an

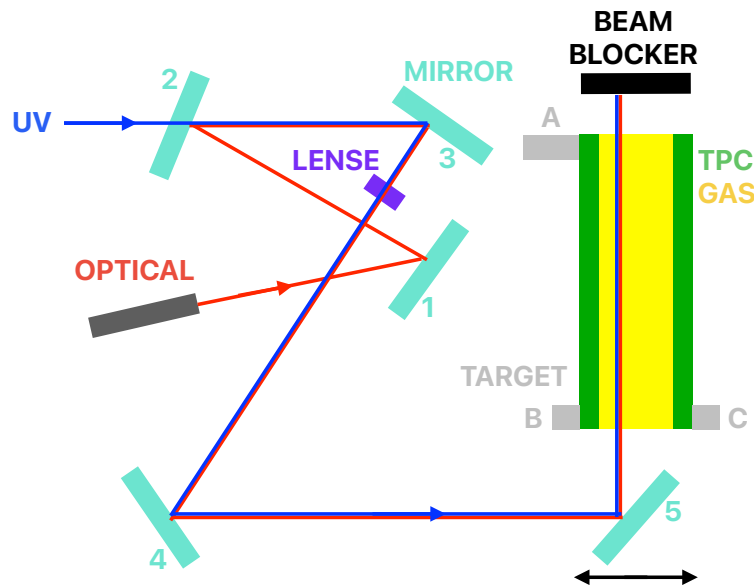


Figure 3.23. Scheme of the laser path to reach the TPC, from above.

optical laser and three small plastic targets mounted outside the TPC, that helped us adjusting the mirrors. The optical laser is convenient in this procedure because it is visible to the naked eye, while the UV laser can be observed only using dedicated visualization tools.

Referring to the labels in Figure 3.23, the first step of the alignment procedure is to align the optical laser with the UV laser using Mirrors 1 and 2. Mirror 2 is installed on a movable mount, which allows to remove it when the UV laser is in use and place it back in position, restoring the original alignment, when the optical laser is needed. We placed an additional target along the path between Mirrors 4

and 5 and we adjusted Mirrors 1 and 2, with the help of a UV detection card³, until the two beams coincided on both the target and the beam blocker at the end of the path.

Once the two lasers are aligned, we aligned the optical laser with respect to the TPC by adjusting Mirrors 3, 4 and 5. The targets mounted outside the TPC, centred with respect to the window, that helped us in this procedure, are shown in Figure 3.24. Notice that Target A, positioned at the end of the chamber relatively to the

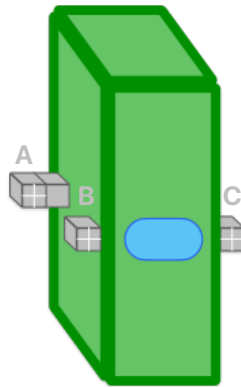


Figure 3.24. A detail on the targets positioning, mounted outside the TPC. The cross engraved on the targets helped us checking both horizontal and vertical alignments.

laser direction, is longer than Target B, allowing us to reach Target A by moving the stage left from Target B. This second part of the procedure begins illuminating the centre of Target B, considered as a reference point, and then, moving the stage to illuminate Target A we could check both vertical and horizontal alignment. Moreover, by illuminating Target C, we could verify that the vertical alignment was preserved for different stage positions. So, first we adjust Mirror 3 by centring the laser on Target B. Then, knowing the distances between the centres of the targets, we move the stage to illuminate Target A, adjusting Mirror 5, and then to Target C, adjusting Mirror 4. By iterating these steps, we were able to align the optical laser with respect to the TPC and, consequently, the UV laser too.

³<https://www.thorlabs.com/thorproduct.cfm?partnumber=VRC1>

3.3 Preparation of the gas mixture

The experimental setup is schematically shown in Figure 3.25 which includes both the electronics and the gas system. The latter is a very important aspect of the

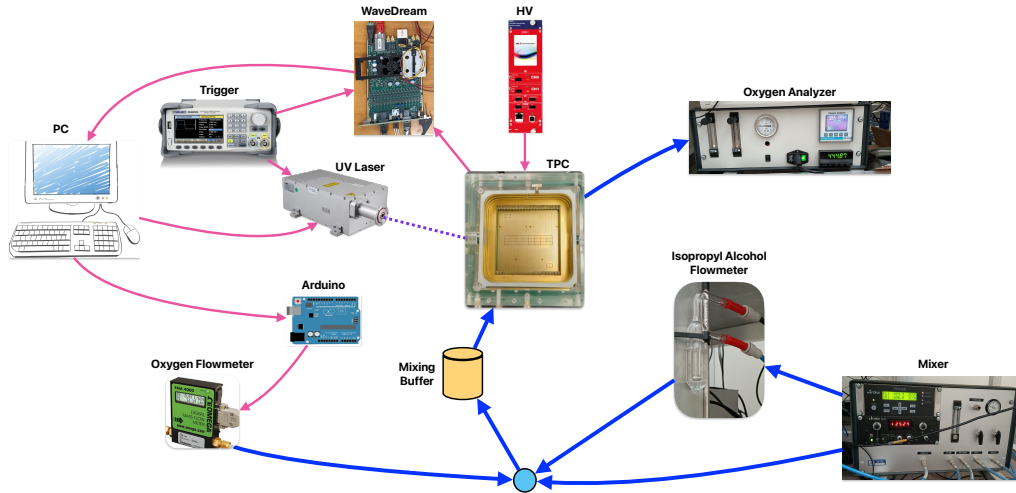


Figure 3.25. Schematic representation of the experimental setup: the blue arrows represent the gas pipes while the pink ones represent the electronic connections.

whole setup which consists of several stages. First, we have a mixer with which we set the ratio between the helium and the isobutane and their total flow. This initial mixture is split in two: one part, referred to as the saturated component, is directed to an analog flowmeter and flows through a bubbler filled with isopropyl alcohol, while the remaining part is kept dry. The fraction of the mixture directed to the saturated component can be adjusted using a manual valve. The two parts then reconnect, together with the oxygen component coming from the electronic oxygen flowmeter, which is controlled by an Arduino board that sets the nominal amount of oxygen that we want to add. The final mixture flows inside an intermediate cylindrical volume with a 1 L capacity, needed to guarantee an homogeneous mixture. Finally, the mixture flows inside the TPC from which it is collected again by the mixer which has a pressure regulation system and a disposal system for the exhausted gas.

The critical point of the preparation is the actual oxygen and isopropyl alcohol concentrations of the mixture, since they affect attachment coefficient and drift velocity, respectively, as better explained in Chapter 4. It is crucial, then, to be in control of these quantities in order for the results to be consistent.

The oxygen concentration monitoring is very straightforward: we placed an

oxygen analyzer downstream, after the chamber, that can measure the oxygen concentration with a 1% uncertainty on the reading.

The isopropyl alcohol concentration, instead, is determined by the fraction of the saturated component over the total flow. Given a total flow Φ_{tot} , which is determined by the helium and isobutane flows, the saturated component flow Φ_{sat} , providing the desired alcohol concentration c , is:

$$\Phi_{sat} = c\Phi_{tot} \frac{P_{atm}}{P_v} \quad (3.2)$$

where P_{atm} is the atmospheric pressure while P_v is the vapor pressure, which reflects the tendency of a substance to transition from the liquid (or solid) phase to the gas phase. P_v (in Torr) can be determined with the Antoine empirical equation[25]:

$$\log_{10}(P_v) = A - \frac{B}{C + T} \quad (3.3)$$

where T (in °C) is the gas temperature while A , B and C are component-specific coefficients. The empirical values of the Antoine coefficients for isopropyl alcohol in the temperature range -10÷90 °C, with P_v expressed in Torr and T in °C, are⁴:

$$A = 8.00308 \quad B = 1505.52 \text{ °C}, \quad C = 211.6 \text{ °C}$$

Substituting these values in Equation 3.3, with an average working temperature of $T = 22.5 \text{ °C}$ and an atmospheric pressure $P_{atm} = 99.5 \text{ kPa} = 746.3 \text{ Torr}$, we find $P_v = 4.98 \text{ kPa} = 37.3 \text{ Torr}$. Using this value in Equation 3.2, considering a total flow $\Phi_{tot} = 100 \text{ sccm}$, which is our working flow, and a concentration $c = 2\%$ we obtain $\Phi_{sat} \simeq 40 \text{ sccm}$.

To calibrate the analog alcohol flowmeter to the corresponding 40 sccm flow, we started by setting a flow rate of 40 sccm on the electronic flowmeter of the mixer. This flow was then directed entirely through the alcohol flowmeter and the observed level was marked on its scale. So, the final mixture was prepared by setting $\Phi_{tot} = 100 \text{ sccm}$ and adjusting the manual valve, in such a way that the saturated flow matches the 40 sccm level marked on the alcohol flowmeter.

⁴<http://ddbonline.ddbst.de/AntoineCalculation/AntoineCalculationCGI.exe>

Chapter 4

Measurements and Data Analysis

This study aims to characterize different variants of the gas mixture used in the MEG II drift chamber, by changing the oxygen concentration and the intensity of the drift field in which our TPC operates. In particular, we are interested in studying mixtures based on helium-isobutane in a 90:10 ratio with the addition of 2% isopropyl alcohol and different oxygen concentrations: 0%, 0.2%, 0.35% and 0.5%. These mixtures are tested under different drift fields, with intensities of 700 V/cm, 1000 V/cm, 1250 V/cm and 1500 V/cm, which is the typical range of the field in the cells of the MEG II drift chamber.

Some critical properties to be measured are drift velocity, attachment coefficient and ageing rate. As already discussed in Chapter 3, the motivations for this study are related to the unreliability of attachment coefficient and ageing rate predictions for this type of mixture, particularly related to the combination of isopropyl alcohol and oxygen, as well as the scarcity of existing literature. Moreover, the results of this study are important not only for a better understanding of the MEG II CDCH, but also for future experiments, as for instance those operating at a future e^+e^- circular collider, which might be interested in mixtures with similar properties.

While the ageing rate measurement will be the subject of a future, dedicated study, in this chapter we are going to present the results of the attachment coefficient and drift velocity measurements, conducted at the Laboratori Nazionali di Frascati (LNF). In Section 1 we are going to explain the adopted experimental procedure, while in Section 2-3 we are going through the data analysis methodologies and results.

1 Experimental Procedure

The data taking procedure adopted consists of few steps. Once the mixture is stable (Section 2.2) and the laser has been aligned (Chapter 3), we can collect different sets of data (runs) by varying the distance of the laser from the readout, which is possible thanks to the fact that Mirror 5 is mounted on a motorized translation stage. The windows of the TPC, through which the laser can reach the gas volume, have a width of 3 cm, so we decided to explore a range of 2 cm in Z in steps of 0.5 cm, starting from the closest distance from the readout that we could access (see Figure 4.1).

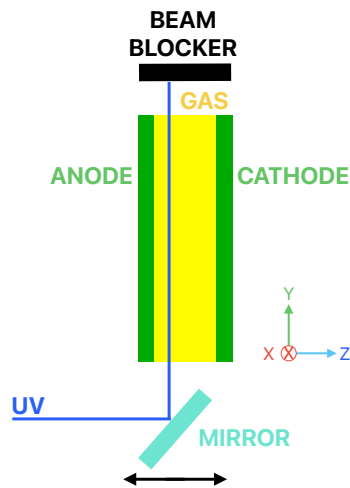


Figure 4.1. A detail of the laser path from above. For reference, in this perspective the anode, hence the readout, is on the left side of the TPC.

We repeated this procedure for each gas mixture and electric field intensity. By analyzing the time of arrival of the signal and the charge collected at different distance of the ionization from the readout, we can measure the drift velocity and the attachment coefficient, respectively, as further explained in Sections 3.1-3.2.

2 Preliminary Tests

Before going through the measurements for the characterizations, it is important to perform some preliminary studies, such as calibrating the electronic flowmeters and checking the mixture stability, meaning to measure the time needed to get a stable mixture when changing from a composition to another.

2.1 Flowmeter Calibration

The first element of the gas system, which is described in Chapter 3, is the mixer that is used to set the proportions of the helium and isobutane flows. It is important to be sure that its electronic flowmeter is correctly calibrated, which can be done exploiting the pressure control system that is integrated in the mixer. The idea is to compare the rate at which the pressure increases in our gas system volume when using only 90 sccm of helium versus 90 sccm of helium combined with 10 sccm of isobutane.

Assuming an ideal gas at constant volume V and temperature T , by taking the time derivative of the ideal-gas law, $PV = nRT$, where P is the pressure, n is the number of moles and R is the universal gas constant, we find:

$$\frac{dP}{dt} = \frac{RT}{V} \frac{dn}{dt} = \frac{RT}{V} \Phi \quad (4.1)$$

where we claim that the variation of number of moles in time is equal to the flux of the gas Φ . However, a leakage in the gas flow may occur, and its effect can be modelled introducing an additional term to the previous relation:

$$\frac{dP}{dt} = \frac{RT}{V} \Phi - f(P) \quad (4.2)$$

where $f(P)$ is the leakage modelling function. By making the reasonable assumption of a leakage function that is linear in pressure $f(P) = kP$, the solution of Equation 4.2 is:

$$P(t) = \frac{RT}{Vk} \Phi + ae^{-kt} = \frac{\tilde{\Phi}}{k} + ae^{-kt} \quad (4.3)$$

where $\tilde{\Phi}$ includes the flux and all the constants. We used this function to fit the data of pressure vs time for both mixtures, as shown in Figure 4.2. Actually we are plotting the difference between the measured pressure P and the atmospheric pressure $P_{atm} = 752$ Torr vs time. Since the volume and the temperature are constant, and hence equal for the two mixtures, by taking the ratio of the $\tilde{\Phi}$ parameters obtained from the fits for the two mixtures, we obtain the helium concentration C_{he} :

$$\frac{\tilde{\Phi}_{he}}{\tilde{\Phi}_{he:iso}} = \left(\frac{RT}{V} \Phi_{he} \right) \left(\frac{V}{RT} \frac{1}{\Phi_{he:iso}} \right) = \frac{\Phi_{he}}{\Phi_{he} + \Phi_{iso}} = C_{he} \quad (4.4)$$

where we used that $\Phi_{he:iso} = \Phi_{he} + \Phi_{iso}$. If the flowmeter is correctly calibrated, we will find a 90% concentration.

We collected three datasets, each consisting of one pressure vs time measurement of the helium mixture and one of the helium-isobutane mixture. The helium concentrations C_{he} found for each dataset are listed in Table 4.1:

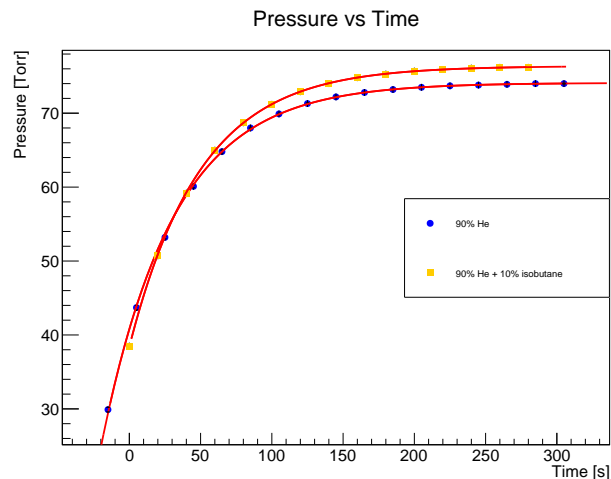


Figure 4.2. A set of calibration curves of the electronic flowmeter.

Dataset N.	C_{He} [%]
1	90 ± 5
2	92 ± 5
3	95 ± 5

Table 4.1. Helium concentration C_{He} obtained from the three datasets. The uncertainties are governed by the systematics: we observed a strong dependence of the fit parameters on the fitting range, leading to an estimated systematic uncertainty of 5%.

By combining all the results we obtain $C_{He} = (92 \pm 5)\%$, where the uncertainty is governed by systematics. The result is compatible with the nominal 90% set of the total flow and it shows that there is no evidence for a miscalibration of the flowmeter inside the mixer.

2.2 Mixture stability

The time necessary to have a stable mixture inside the TPC, after having changed the set point of the oxygen concentration, was studied using the oxygen analyzer. We started with the calibration of the analyzer, that is performed by flowing ambient air through it, and adjusting its readout to get 20.9%, that is the nominal oxygen concentration in air. The procedure was repeated at different times to verify the stability of the calibration. Then, we connected the analyzer to our gas system, downward with respect to the TPC, and we let it clean up from all the oxygen, flowing the pure mixture with the addition of the isopropyl alcohol. We were able

to reach the minimum level of 120 ppm of oxygen.

At this point, we set the nominal oxygen concentration to be added to the mixture through the Arduino board that regulates the electronic oxygen flowmeter and then we monitored how the oxygen concentration evolved in time, reading the measurement of the oxygen analyzer.

The plots shown in Figure 4.3 are very important since we can understand how long the mixture takes to reach a composition stability, in order for the signal to be stable and the measurements to be reliable. In particular, we can see that the transition from one mixture to another needs about one hour before it reaches the composition stability needed for our measurements.

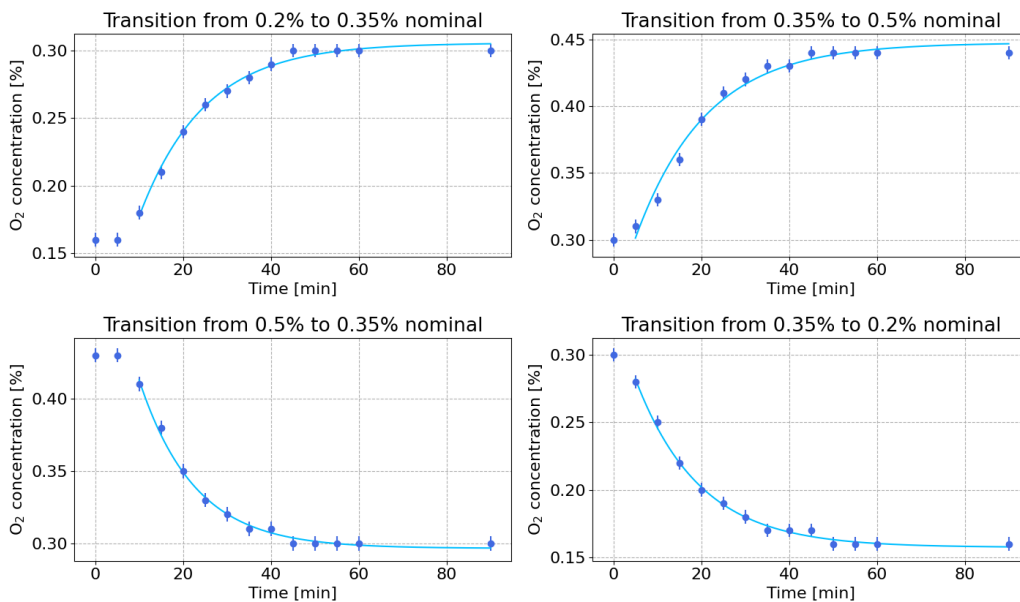


Figure 4.3. The transition of the mixture composition from one oxygen concentration to another in four different cases. The first points are left out from the fit since the transition has not yet begun.

Data are fitted with an exponential function that describes the relation between the oxygen concentration C_{O_2} and time t :

$$C_{O_2} = Ae^{-kt} + c \quad (4.5)$$

where A , k and c are free parameters. In particular, k is related to the characteristic timescale of the curves τ , through the relation $k = 1/\tau$, while c is the concentration reached by the mixture when it settles. The characteristic time τ is expected to correspond to the time needed to exchange a volume of gas equal to the total volume

that is filled by the mixture. The total volume is given by the mixing buffer (1 L) plus the TPC (0.5 L) so it has a capacity of 1.5 L. With a total flow of 100 sccm, $\tau \sim 15$ min, in agreement with the values obtained from the different fits, as shown in Table 4.2. Since the mixture takes one hour to become stable, it means that it is necessary to exchange at least four volumes of gas.

Transition	A [%]	τ [s]	c [%]	χ^2/dof
0.2% \rightarrow 0.35%	-0.25(1)	14.81958(2)	0.306(2)	0.52
0.35% \rightarrow 0.5%	-0.20(1)	16.15234(2)	0.447(4)	1.6
0.5% \rightarrow 0.35%	0.26(1)	12.59637(3)	0.230(2)	0.37
0.35% \rightarrow 0.2%	0.175(5)	14.60152(2)	0.157(2)	0.31

Table 4.2. Fit parameters of the evolution of the oxygen concentration in four different transitions.

We want to point out that there is a mismatch between the nominal oxygen concentrations set through the Arduino board, indicated in the title of each plot, and the initial and final stable points of the mixture. However, since we calibrated the oxygen analyzer, we decided to rely on its measurements rather than on what we set through the Arduino board. We can model the mismatch with a straight line that calibrates the Arduino board, as shown in Figure 4.4. So, the values of the oxygen concentration that we will consider from now on for our measurements are the values that we read from the oxygen analyzer.

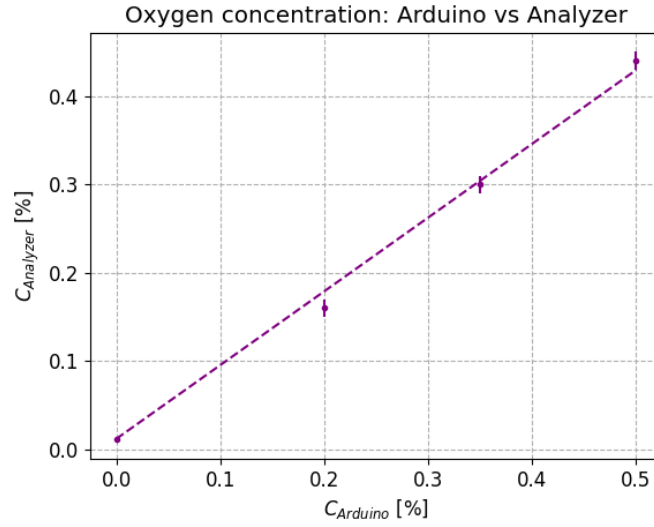


Figure 4.4. Calibration for the Arduino set point. The fit function is $y = mx + q$, where $m = 0.8352(2)$, $q = 0.011874(1)$ and $\chi^2/dof = 2.44$.

3 Data analysis

Data are divided into runs: each run contains a thousand of events, each of which is composed by the signals of the eight channels of the WaveDream, as shown in Figure 4.5. With a 700 MSPS acquisition rate, the acquisition window lasts ~ 1428 ns per event.

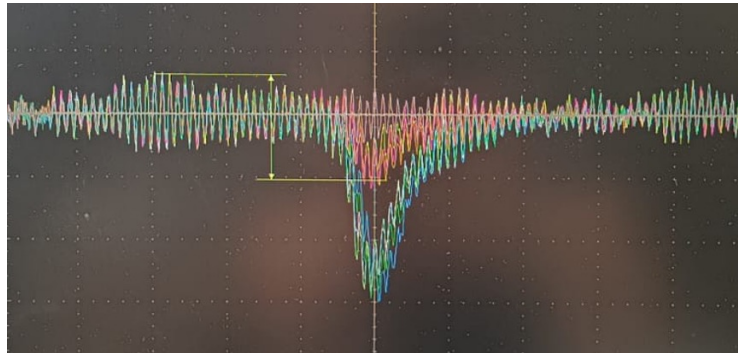


Figure 4.5. An example of an event signal for the eight channels of the WaveDream: the larger signals corresponds to the pads in the central row, right below the laser beam, while smaller signal corresponds to the pads in the upper row.

Channel 2 is far from the region illuminated by the laser, and hence we expect no signal in this channel, but it is affected by the same ambient noise as the other channels. For this reason, it can be used for common noise subtraction through a

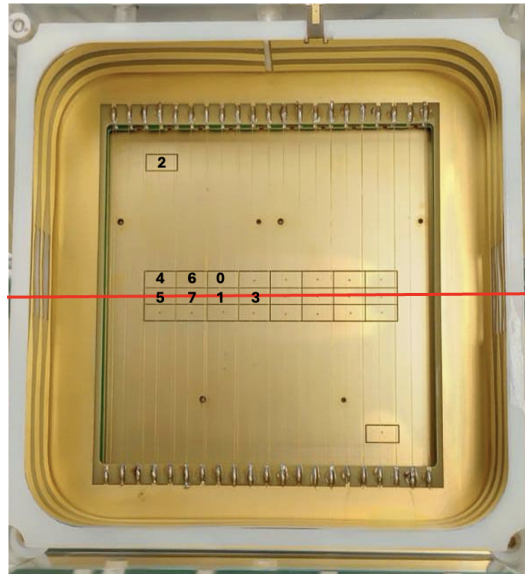


Figure 4.6. A picture of the inside of the TPC as a reference for the relation between the channels of the WaveDream and the readout pads. The red line represents the laser beam.

point-to-point subtraction algorithm in which the readout of channel 2 is subtracted to the readout of the other channels at each time point. An example of the result of this algorithm is shown in Figure 4.7. In this way we are able to remove the main noise frequencies, as shown in Figures 4.8-4.9. To further clean the signal, we performed a low-pass filter on the Fast Fourier Transform (FFT) with a cut-off frequency at 200 MHz, as shown in an example in Figure 4.10.

After this preliminary manipulation of the data, we studied the deposited charge and time of arrival (TOA) distributions for each run and per channel, as shown in the example in Figure 4.11. The deposited charge is calculated by first selecting a region where the signal remains above the baseline for at least 70 ns. The baseline, calculated as the mean amplitude over the last 200 ns of acquisition (a region where no signal is expected), is then subtracted from the selected points, and finally we compute the integral within this region. The TOA, instead, is evaluated as the time when the signal crosses a level of 20% of its maximum amplitude after the baseline subtraction.

From these distributions it is possible to obtain the mean value of the charge deposited per channel, used for the attachment coefficient evaluation, and the mean value of the TOA per channel, used for the drift velocity evaluation. The uncertainties are assigned as the standard deviation of the distribution divided by the square root

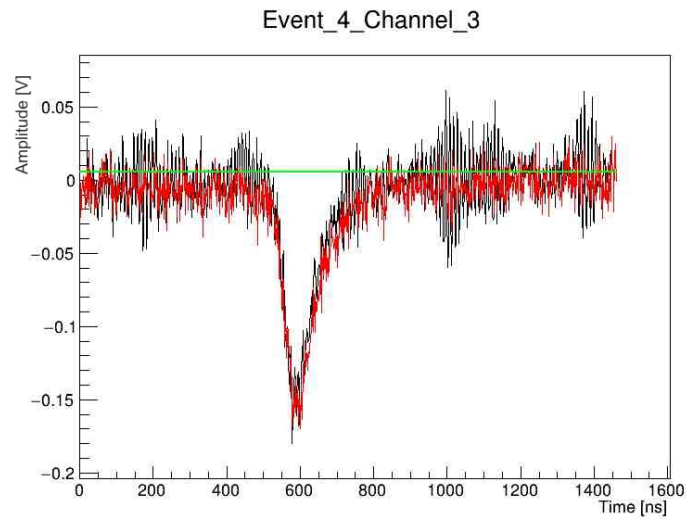


Figure 4.7. An example of the signal after the noise subtraction (red) superimposed to the raw signal (black).

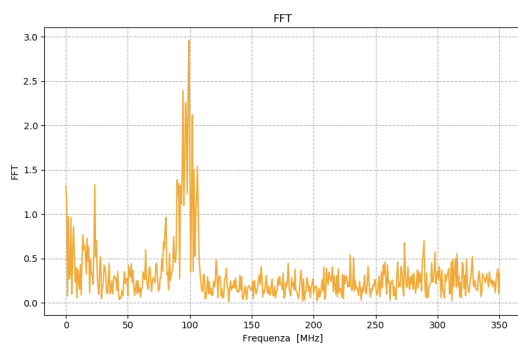


Figure 4.8. FFT of the signal before the noise subtraction.

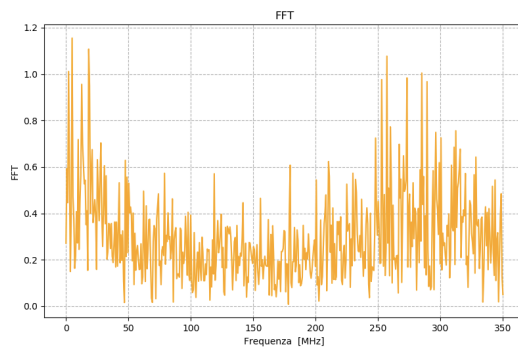


Figure 4.9. FFT of the signal after the noise subtraction.

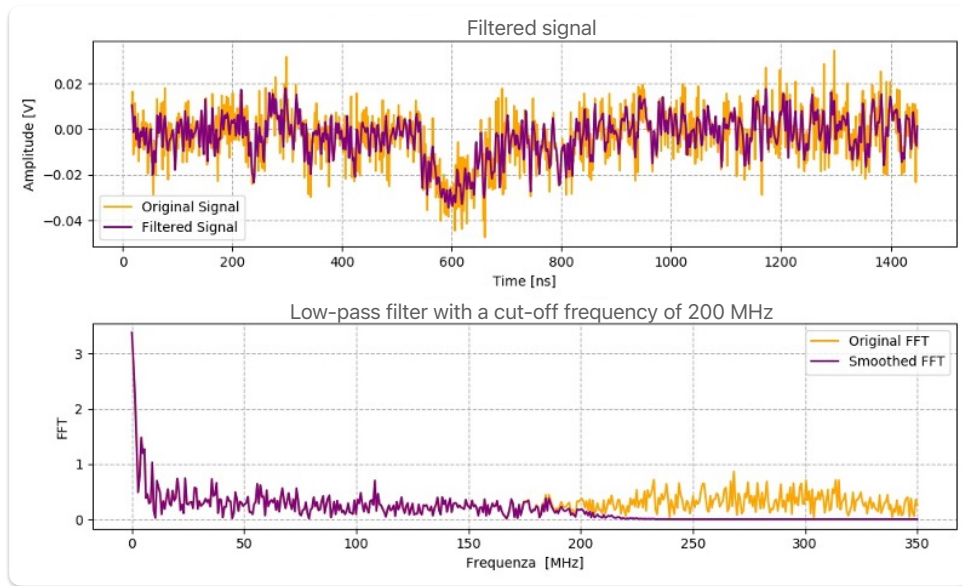


Figure 4.10. An example of the effect of the low-pass filter on a signal.

of the number of events.

We wanted to understand if possible instabilities of the laser can affect the mean TOA and mean charge evaluation. The idea was to repeat several acquisitions at different times with the same conditions (same laser intensity and position and same mixture). From the results shown in Figure 4.12, we do not have any evidence for instabilities in time. However, the ordering of the channels in the TOA plot shows a trend that might be due to a small field inhomogeneity: the TOA increases for channels corresponding to more lateral pads. A closer look at the central region of the ANSYS simulations reveals a slight inhomogeneity in the electric field moving away from the centre of the TPC, as shown in Figures 4.13-4.14. We expect, then, to find a similar trend also on the drift velocity.

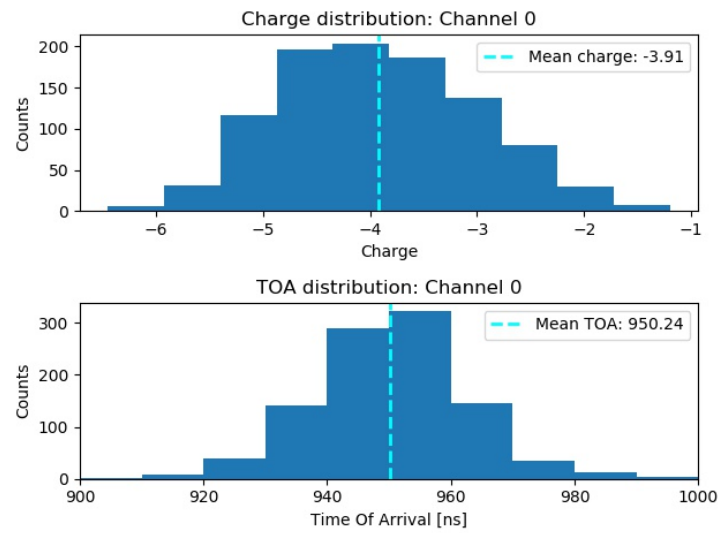


Figure 4.11. Example of the charge and TOA distributions for a specific channel of a run.

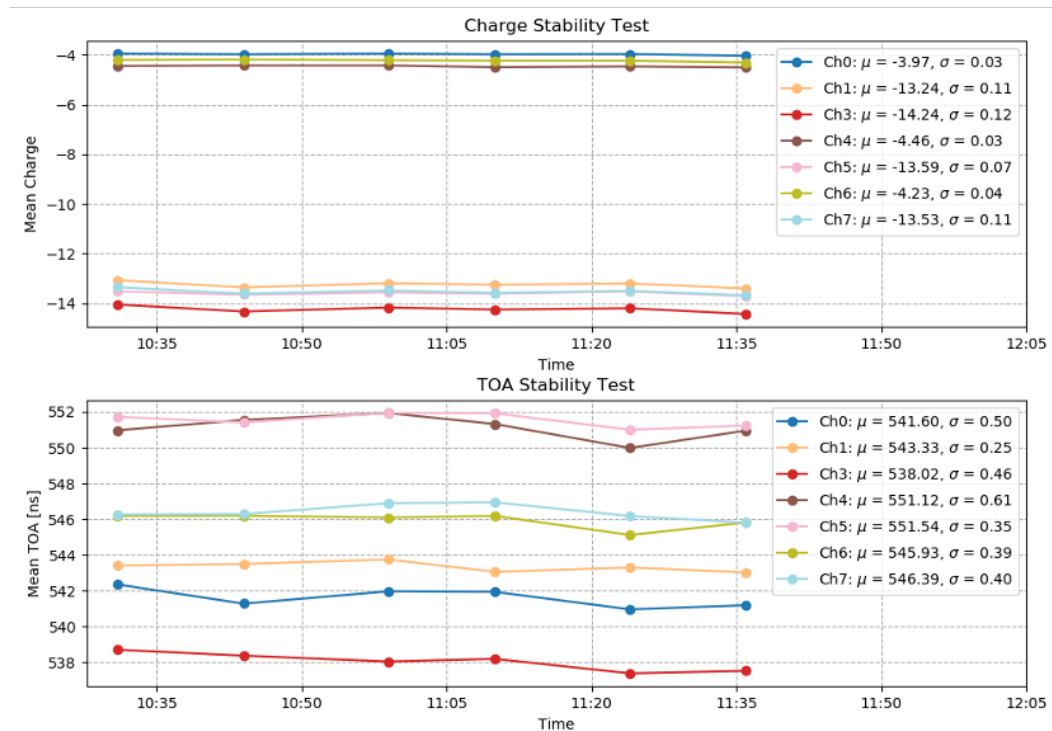


Figure 4.12. A study of the stability of TOA and charge measurement with same conditions at different times.

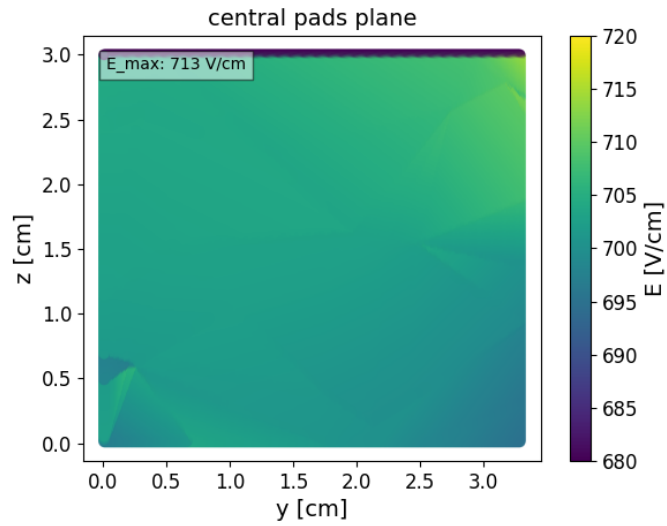


Figure 4.13. Simulation of the electric field on the vertical plane above the central row of pads, corresponding to channels 1, 3, 5 and 7.

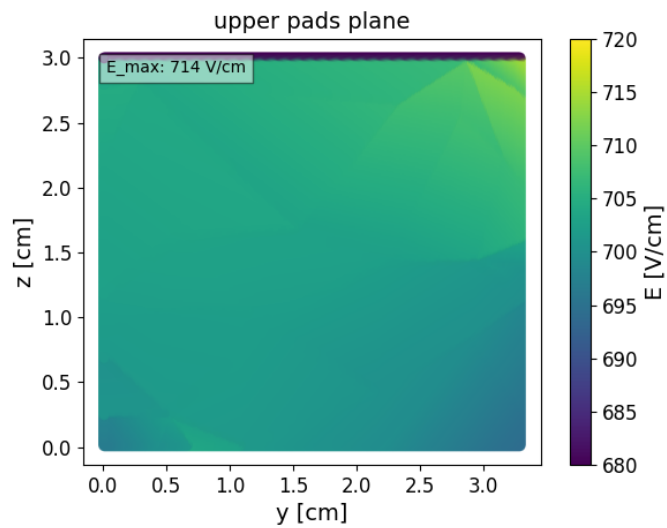


Figure 4.14. Simulation of the electric field on the vertical plane above the upper row of pads, corresponding to channels 0, 4 and 6.

3.1 Drift velocity

When a gas is ionized in the presence of an electric field, the ionized electrons and ions drift along the electric field lines and their average velocity is called drift velocity. We will focus on the electron drift velocity, which from now on we will refer to as just drift velocity.

As explained in Section 3, for each run, we were able to extract the mean of the TOA distribution, and knowing the laser position for a specific run, it is possible to fit our data with a straight line:

$$z = v_{drift}T + q \quad (4.6)$$

where z is the Z position of the laser beam, T is the TOA, q takes into account offsets in time and position (whose zeros are arbitrarily chosen in our setup) and the slope of the curve gives the drift velocity. Some examples of fits of the drift velocities are shown in Figures 4.15-4.16. Fit parameters can be found in Appendix A.

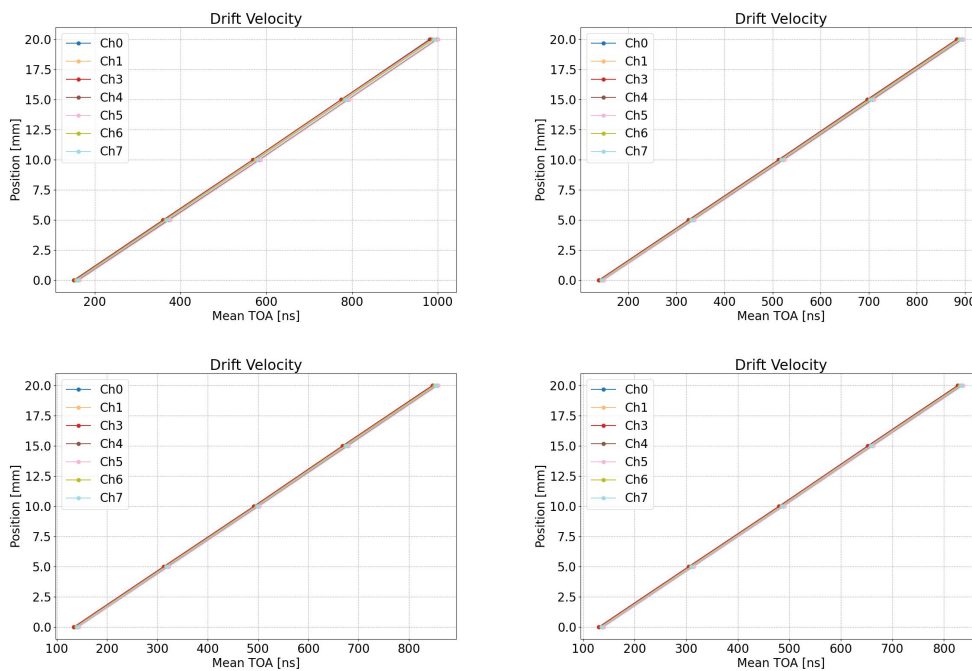


Figure 4.15. A comparison of drift velocities in the case of a mixture with 0% oxygen at different drift field. From the top left to the bottom right the considered drift fields are 700 V/cm, 1000 V/cm, 1250 V/cm and 1500 V/cm. The fit function is $z = v_{drift}T + q$.

As pointed out in Section 3, we expect a trend of the drift velocity with respect to the position of the pad. To highlight this behaviour, we realized a 3D histogram, shown in Figure 4.17, in which the horizontal plane represents the position of the

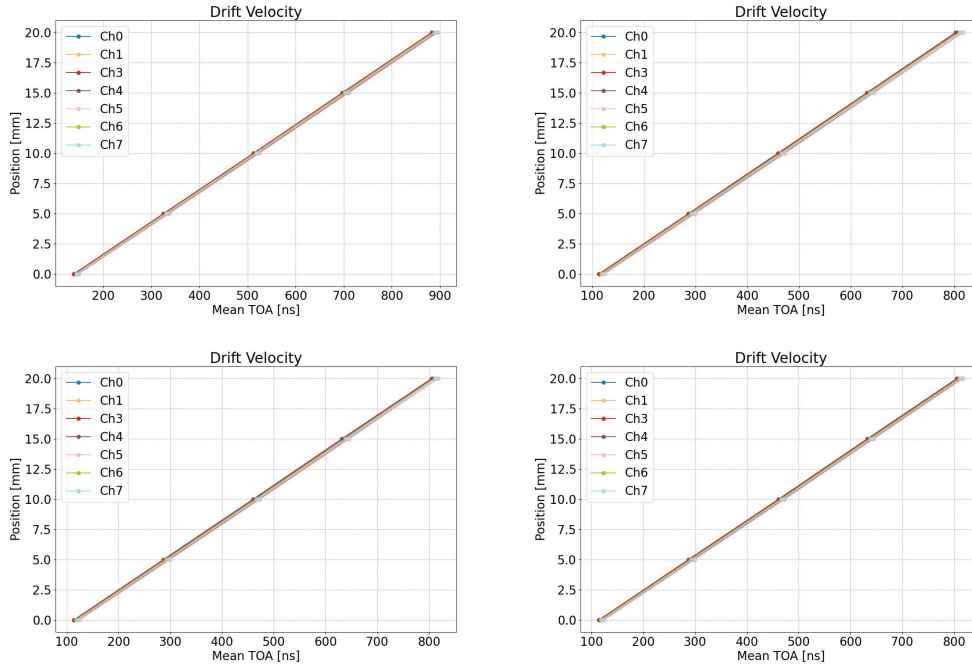


Figure 4.16. A comparison of drift velocities with a drift field of 1000 V/cm for different mixtures. From the top left to the bottom right the mixtures have 0%, 0.16%, 0.3% and 0.44% of oxygen concentration. The fit function is $z = v_{drift}T + q$.

pads inside the TPC while the height of the bins represents an average drift velocity obtained combining different runs. The decreasing trend of the drift velocity as more external pads are considered, is compatible with the small inhomogeneity of the electric field in the central region shown in Figures 4.13-4.14. Given that, from now on we will consider only the values obtained from the most central pad, corresponding to channel 3.

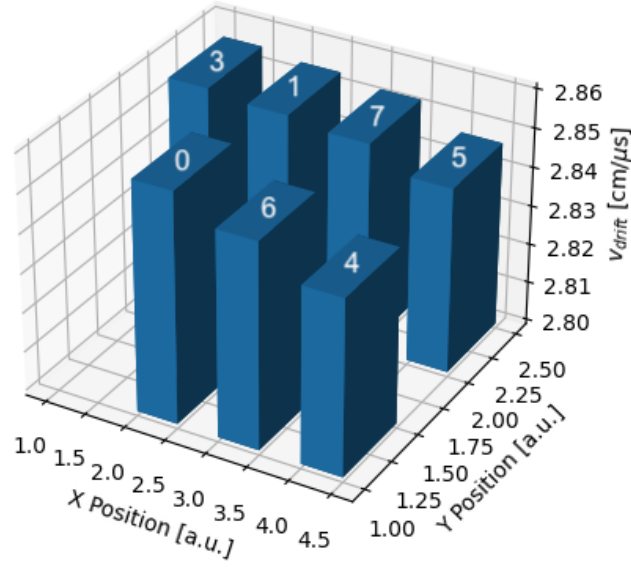


Figure 4.17. Spatial distribution of the drift velocity. A correlation with the spatial coordinates is evident, considering the centre of the TPC at the top left corner.

Collecting the results from our data, we studied how the drift velocity depends on the electric field, as shown in Figure 4.18. Data are fitted with a quadratic function and the parameters obtained are shown in Table 4.3. As expected, we observed that the drift velocity increases with the drift field. Moreover, as previously mentioned, the drift velocity depends also on the mixture composition: a 2% variation introduced by the addition of isopropyl alcohol is expected to significantly alter the curve, while changes in oxygen concentration result in only minor variations in the mixture composition, and thus, are not expected to significantly impact the behaviour.

Mixture	a [$\text{cm}^3/(\text{V}^2\mu\text{s})$]	b [$\text{cm}^2/(\text{V}\mu\text{s})$]	c [$\text{cm}/\mu\text{s}$]	χ^2/dof
1	$-6.5(6)\cdot 10^{-7}$	$2.0(1)\cdot 10^{-3}$	1.31(7)	1.5
2	$-1.24(7)\cdot 10^{-6}$	$3.9(2)\cdot 10^{-3}$	0.23(8)	2.7
3	$-1.16(8)\cdot 10^{-6}$	$3.7(2)\cdot 10^{-3}$	0.38(9)	1.9
4	$-1.09(8)\cdot 10^{-6}$	$3.5(2)\cdot 10^{-3}$	0.51(8)	1.5

Table 4.3. Fit parameter of the curves in Figure 4.18: the fit function is $v_d = aE^2 + bE + c$.

Mixture 1: helium-isobutane 90:10.

Mixture 2: helium-isobutane 90:10 + 2% isopropyl alcohol + 0.16% O_2 .

Mixture 3: helium-isobutane 90:10 + 2% isopropyl alcohol + 0.30% O_2 .

Mixture 4: helium-isobutane 90:10 + 2% isopropyl alcohol + 0.44% O_2 .

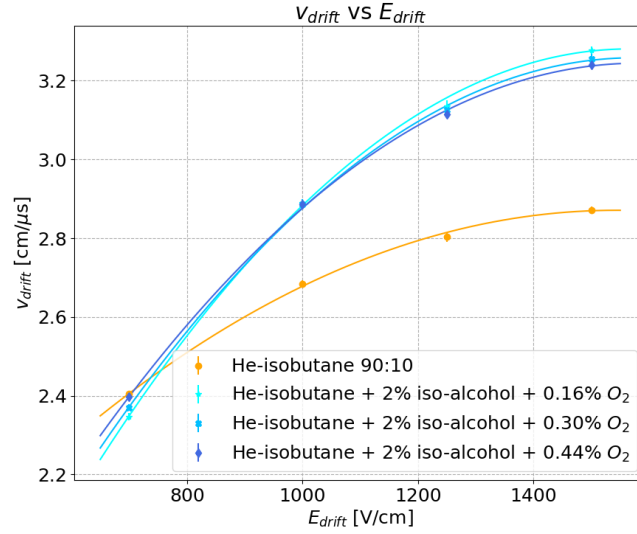


Figure 4.18. Drift velocity as a function of the drift field. The fit function is quadratic as suggested by the Golovatyuk et al. study[2].

3.2 Attachment coefficient

The attachment coefficient quantifies the tendency of a gas to capture electrons and happens when a mixture has an electronegative component, like the oxygen. Since our mixtures have a small concentration of oxygen, we expect to observe this phenomenon. In particular, what happens is that when the laser ionizes the gas, the ionized electrons drift toward the anode but some of them are captured by the oxygen and this suppresses the signal.

To measure the attachment, we study the relation between the Z position of the laser and the collected charge, which is determined by the number of electrons reaching the readout. It is in our interest, then, to study how such suppression is related to the oxygen concentration but also to the drift field, since the faster the electrons the lower the probability to be captured by the oxygen atoms.

Drifting electrons have a given probability η of being captured per unit length. Consequently the number N of electrons reaching the readout will be:

$$N(d) = N_0 e^{-\eta d} \quad (4.7)$$

where d is the drift distance and N_0 is the number of ionizations, which also absorbs the position offset along the Z direction:

$$N_0 e^{-\eta d} = N_0 e^{-\eta(z-z_0)} \propto e^{-\eta z} \quad (4.8)$$

The charge measured at the readout will follow exactly the same trend of the number of ionizations N . Some examples of the fit in logarithmic scale are shown in Figures 4.19-4.20. Fit parameters can be found in Appendix A.

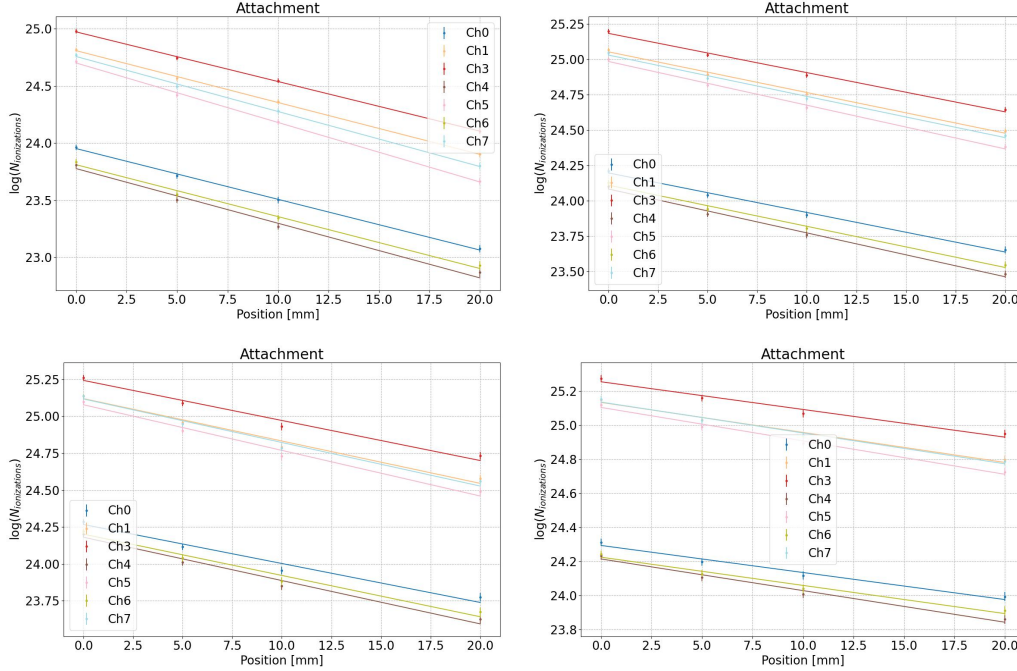


Figure 4.19. A comparison of attachment coefficients in the case of a mixture with 0.16% oxygen at different drift field. From the top left to the bottom right the considered drift fields are 700 V/cm, 1000 V/cm, 1250 V/cm and 1500 V/cm. The fit function is $\ln(N) = -\eta z + q$ where $q = \ln(N_0)$.

Similarly to what we saw in Section 3.1, we found a spatial trend for the attachment coefficient, shown in Figure 4.21, that is compatible with what we observed in Figure 4.17 for the drift velocity. If the electric field is slightly inhomogeneous, and in particular decreases moving from the centre, this means that electrons that drift in a more external region move slower so they are more likely to be captured by the oxygen, resulting in a larger attachment coefficient. For the same reason expressed in the case of the drift velocity, we are going to present our results focusing only on channel 3, which is the most central one.

Once the attachment coefficients have been extrapolated from our data, we can study how they depend on the drift field and the oxygen concentration. In Figure 4.22 we show the attachment coefficient versus the drift field for the different oxygen concentrations. The same measurements are shown in Figure 4.23 versus the oxygen concentration at different drift fields. The trends are fitted with an hyperbole and a

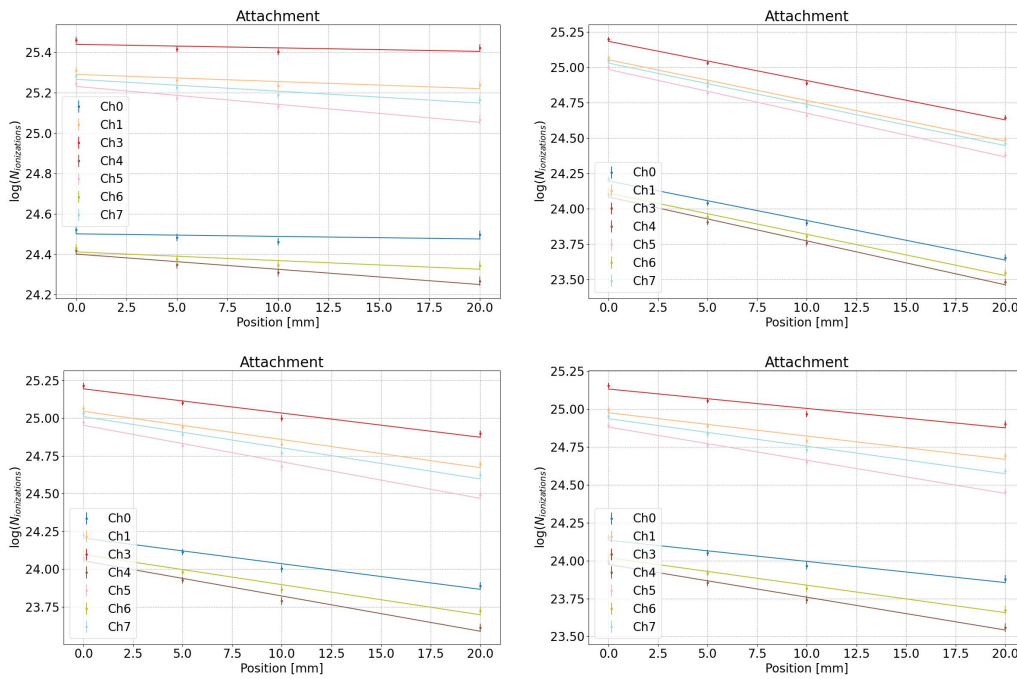


Figure 4.20. A comparison of attachment coefficients with a drift field of 1000 V/cm for different mixtures. From the top left to the bottom right the mixtures have 0%, 0.16%, 0.3% and 0.44% of oxygen concentration. The fit function is $\ln(N) = -\eta z + q$ where $q = \ln(N_0)$.

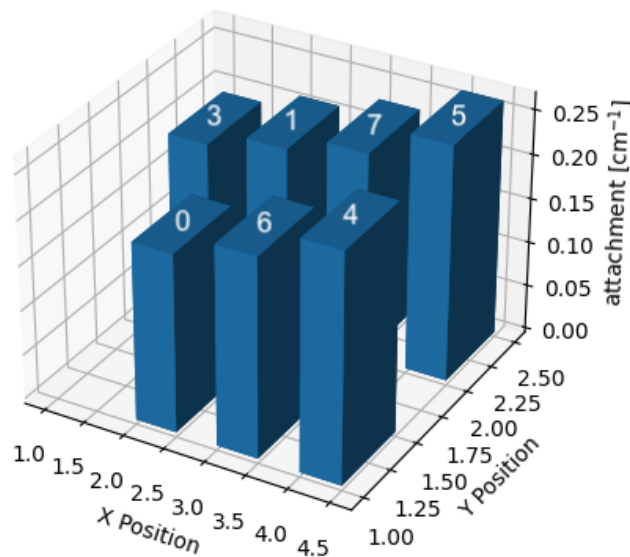


Figure 4.21. Spatial distribution of the attachment coefficient. There is a clear correlation with the position of the pads. The centre of the TPC is located at the top left corner.

straight line, respectively, whose fit-parameters are shown in Tables 4.4-4.5.

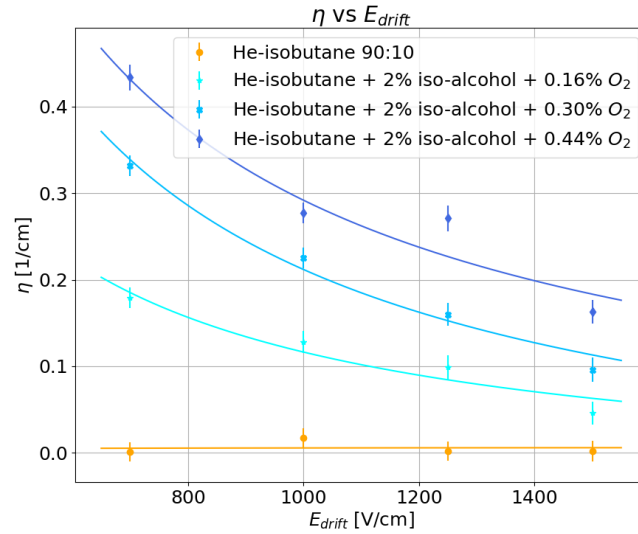


Figure 4.22. Attachment coefficient as a function of the drift field at fixed mixture. The fit function is an hyperbole as suggested in the Golovatyuk et al. work[2].

Mixture	a [V/cm ⁻²]	b [cm ⁻¹]	χ^2/dof
1	-1(2)	6(2)·10 ⁻³	0.72
2	1.6(2)·10 ²	-4(2)·10 ⁻²	1.9
3	3.0(2)·10 ²	-8(2)·10 ⁻²	1.7
4	3.3(2)·10 ²	-3(2)·10 ⁻²	6.2

Table 4.4. Fit parameter of the curves in Figure 4.22: the fit function is $\eta = \frac{a}{E} + b$.

Mixture 1: helium-isobutane 90:10.

Mixture 2: helium-isobutane 90:10 + 2% isopropyl alcohol + 0.16% O₂.

Mixture 3: helium-isobutane 90:10 + 2% isopropyl alcohol + 0.3% O₂.

Mixture 4: helium-isobutane 90:10 + 2% isopropyl alcohol + 0.44% O₂.

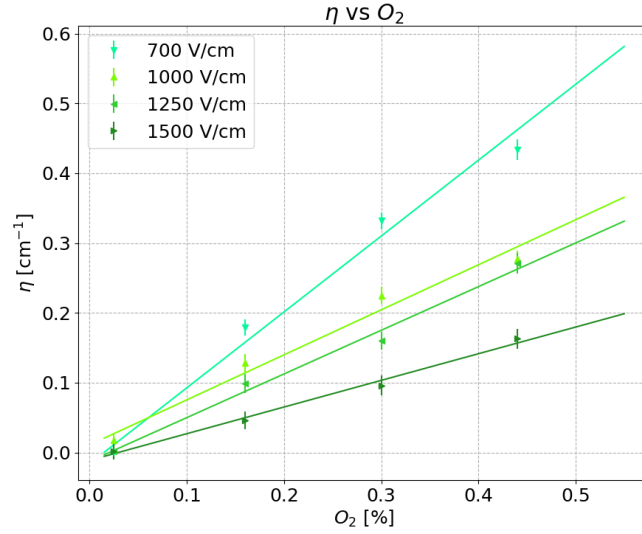


Figure 4.23. Attachment coefficient as a function of the oxygen concentration at fixed drift field. Data are fitted with a straight line as suggested in the Golovatyuk et al. work[2].

$E_{drift}[V/cm]$	$a [V^{-1}]$	$b [cm^{-1}]$	χ^2/dof
700	1.09(5)	$-1(1) \cdot 10^{-2}$	5.4
1000	0.64(4)	$1(1) \cdot 10^{-3}$	3.5
1250	0.62(4)	$-1(1) \cdot 10^{-2}$	1.2
1500	0.38(1)	$-1(1) \cdot 10^{-2}$	0.33

Table 4.5. Fit parameters of the curves in Figure 4.23: the fit function is $\eta = aC_{O_2} + b$.

3.3 Garfield comparison

Since the literature does not provide many studies for similar mixtures, to check the consistency of our results we performed some **Garfield++** simulations. In the **Garfield++** environment it is possible to define a mixture by specifying its components and their proportions. The four considered mixtures, with renormalized concentrations (adding up to 100%), are: helium-isobutane 90:10; helium 88.09%, isobutane 9.79%, isopropyl alcohol 1.96%, oxygen 0.16%; helium 87.98%, isobutane 9.78%, isopropyl alcohol 1.95%, oxygen 0.29%; helium 87.86%, isobutane 9.76%, isopropyl alcohol 1.95%, oxygen 0.43%. It is then possible to estimate the electron drift properties and in particular the simulated drift velocity and attachment coefficient in a given electric field. In Figures 4.24-4.25-4.26, we reproduced the plots already

shown in Figures 4.18-4.22-4.23, respectively, using the simulated data. The general behaviours of each plot is well reproduced by the same fit-function model of our data but there are significant differences in the scales.

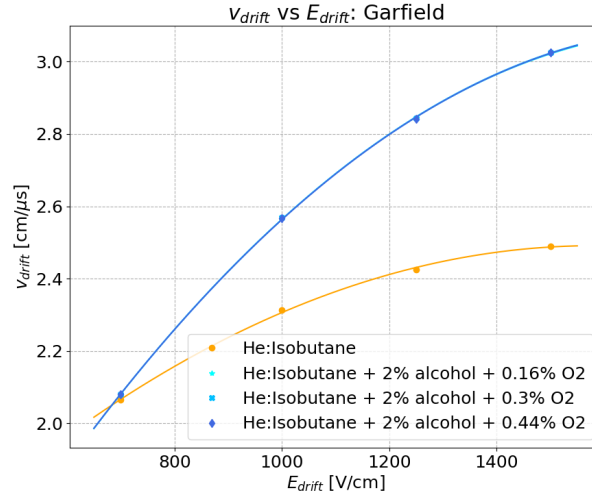


Figure 4.24. Drift velocity as a function of the drift field obtained from Garfield++ simulation. Simulated data are fitted with a quadratic function.

Mixture	a [$\text{cm}^3/(\text{V}^2\mu\text{s})$]	b [$\text{cm}^2/(\text{V}\mu\text{s})$]	c [$\text{cm}/\mu\text{s}$]	χ^2/dof
1	$-5.5(7)\cdot 10^{-7}$	$1.7(1)\cdot 10^{-3}$	1.12(8)	0.97
2	$-8.7(3)\cdot 10^{-7}$	$3.08(7)\cdot 10^{-3}$	0.35(4)	0.22
3	$-8.6(4)\cdot 10^{-7}$	$3.0(1)\cdot 10^{-3}$	0.35(5)	0.42
4	$-8.6(4)\cdot 10^{-7}$	$3.0(1)\cdot 10^{-3}$	0.36(5)	0.42

Table 4.6. Fit parameter of the curves in Figure 4.24: the fit function is $v_d = aE^2 + bE + c$.

Mixture 1: helium-isobutane 90:10.

Mixture 2: helium-isobutane 90:10 + 2% isopropyl alcohol + 0.16% O_2 .

Mixture 3: helium-isobutane 90:10 + 2% isopropyl alcohol + 0.3% O_2 .

Mixture 4: helium-isobutane 90:10 + 2% isopropyl alcohol + 0.44% O_2 .

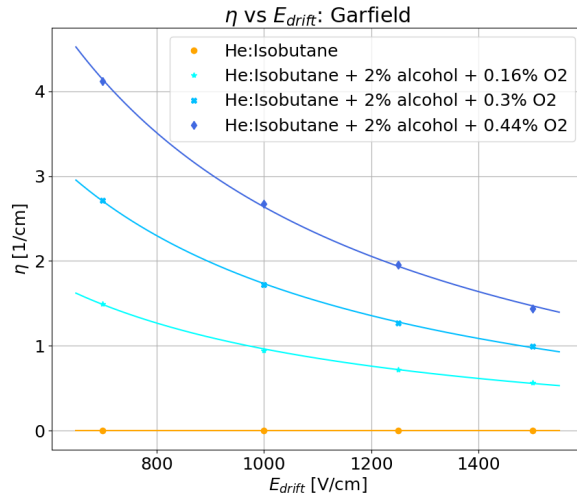


Figure 4.25. Attachment coefficient as a function of the drift field obtained from `Garfield++` simulation. Simulated data are fitted with a hyperbole.

Mixture	a [V/cm ⁻²]	b [cm ⁻¹]	χ^2/dof
1	N.A.	N.A.	N.A.
2	$1.22(2) \cdot 10^3$	-0.26(3)	2.2
3	$2.27(1) \cdot 10^3$	-0.53(3)	3.5
4	$3.50(2) \cdot 10^3$	-0.86(7)	8.3

Table 4.7. Fit parameter of the curves in Figure 4.25: the fit function is $\eta = \frac{a}{E} + b$.

Mixture 1: helium-isobutane 90:10.

Mixture 2: helium-isobutane 90:10 + 2% isopropyl alcohol + 0.16% O₂.

Mixture 3: helium-isobutane 90:10 + 2% isopropyl alcohol + 0.3% O₂.

Mixture 4: helium-isobutane 90:10 + 2% isopropyl alcohol + 0.44% O₂.

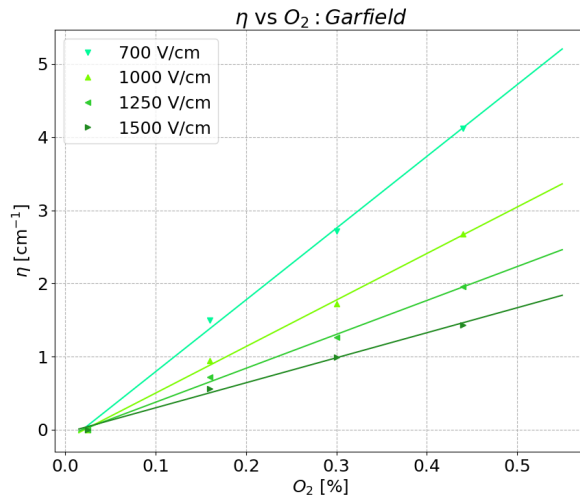


Figure 4.26. Attachment coefficient as a function of the oxygen concentration obtained from Garfield++ simulation. Simulated data are fitted with a straight line.

$E_{drift}[V/cm]$	$a [V^{-1}]$	$b [cm^{-1}]$	χ^2/dof
700	9.80(9)	-0.185(7)	8.9
1000	6.35(4)	-0.133(3)	3.6
1250	4.63(3)	-0.086(3)	3.2
1500	3.42(3)	-0.041(3)	3.2

Table 4.8. Fit parameters of the curves in Figure 4.26: the fit function is $\eta = aE + b$.

Previous studies on similar mixtures[2] already showed that Garfield++ is not able to appropriately simulate electron collisions in complex molecules, resulting in the wrong prediction on the attachment coefficient. However, the incompatibility between the drift velocity plots (Figure 4.18 and Figure 4.24) is more surprising, since previous measurements with the pure helium-isobutane mixture are in good agreement with Garfield++[26]. It can indicate some systematic uncertainties in our measurements, that will need further investigations in the future.

Moreover, we suspect that our data may be affected by saturation effects: when the signal amplification exceeds a certain threshold, the system becomes non-linear. This occurs because avalanches carrying a large charge generate ion clouds that partially shield the electric field. To determine if and how to correct for this effect, we will investigate how the signal varies with different amplification gains, which are controlled by the laser intensity and the tension of the sense wires.

Conclusions

The work presented in this thesis led to the measurement of the drift velocity and attachment coefficient for different gas mixtures based on the composition used in the MEG II drift chamber. In particular, four mixtures were studied: one consisting of pure helium-isobutane in a 90:10 ratio and three others based on helium-isobutane 90:10 with the addition of 2% of isopropyl alcohol and different concentrations of oxygen (0.16%, 0.30%, 0.44%).

The characterization was carried out using a small TPC, specifically designed for this project, illuminated by a UV laser. Simulations of the electric field inside the TPC were performed to assess its homogeneity. We found that the structural features of the TPC do not generate discharges within the operational range, however, despite the small active volume, the absence of a field cage slightly compromises the homogeneity of the electric field within the gas volume. For this reason, we focused on the results obtained from the most central pad, corresponding to channel 3 of the WaveDream board. After obtaining the positive simulation results, we proceeded with assembling the setup, which involved constructing the TPC, aligning the laser, establishing the electronic and gas connections, and calibrating the alcohol, the oxygen and the helium-isobutane flowmeters.

For each gas mixture we illuminated the TPC under different electric fields to study the dependence of the drift velocity and attachment coefficient on the mixture composition and field intensity. The results obtained are compatible with our expectations, as both drift velocity and attachment coefficient follow the functional dependencies indicated in our reference[2]. However, we observed a discrepancy when comparing these results to the corresponding `Garfield++` simulations. Although the trends are consistent (both measured and simulated data can be described by the same functional form), the scale differs significantly, with our measurements larger than the simulations. While it is well-known that `Garfield++` simulations for the attachment coefficient are not reliable, the disagreement in drift velocity results was unexpected. Previous measurements using the pure helium-isobutane mixture

showed good agreement with **Garfield++** simulations[26]. This discrepancy suggests the presence of systematic uncertainties in our measurements, which require further investigation in the future.

Appendix A

Fit-parameters tables

Tables A.1-A.2-A.3-A.4 present the fit parameters corresponding to Figures 4.15-4.16-4.19-4.20, respectively.

In the tables, the mixtures are referred to as Mixture 1, 2, 3, and 4, which correspond to the following compositions:

- Mixture 1: helium-isobutane 90:10
- Mixture 2: helium-isobutane 90:10 + 2% isopropyl alcohol + 0.16% O₂
- Mixture 3: helium-isobutane 90:10 + 2% isopropyl alcohol + 0.30% O₂.
- Mixture 4: helium-isobutane 90:10 + 2% isopropyl alcohol + 0.44% O₂.

E [V/cm]	Ch	Fit Parameters	E [V/cm]	Ch	Fit Parameters
700	0	$v_{drift} = 2.408(4) \text{ cm}/\mu\text{s}$ $q = -3.66(2) \text{ mm}$ $\chi^2 = 1.80$	1000	0	$v_{drift} = 2.689(4) \text{ cm}/\mu\text{s}$ $q = -3.74(2) \text{ mm}$ $chi^2 = 0.89$
	1	$v_{drift} = 2.403(3) \text{ cm}/\mu\text{s}$ $q = -3.76(2) \text{ mm}$ $\chi^2 = 1.74$		1	$v_{drift} = 2.685(3) \text{ cm}/\mu\text{s}$ $q = -3.84(2) \text{ mm}$ $chi^2 = 1.06$
	3	$v_{drift} = 2.406(3) \text{ cm}/\mu\text{s}$ $q = -3.66(2) \text{ mm}$ $\chi^2 = 0.84$		3	$v_{drift} = 2.686(3) \text{ cm}/\mu\text{s}$ $q = -3.73(2) \text{ mm}$ $chi^2 = 1.09$
	4	$v_{drift} = 2.389(3) \text{ cm}/\mu\text{s}$ $q = -3.90(2) \text{ mm}$ $\chi^2 = 4.92$		4	$v_{drift} = 2.678(4) \text{ cm}/\mu\text{s}$ $q = -3.96(2) \text{ mm}$ $chi^2 = 1.71$
	5	$v_{drift} = 2.391(3) \text{ cm}/\mu\text{s}$ $q = -3.97(2) \text{ mm}$ $\chi^2 = 5.34$		5	$v_{drift} = 2.676(3) \text{ cm}/\mu\text{s}$ $q = -4.01(2) \text{ mm}$ $chi^2 = 2.15$
	6	$v_{drift} = 2.399(3) \text{ cm}/\mu\text{s}$ $q = -3.76(2) \text{ mm}$ $\chi^2 = 1.90$		6	$v_{drift} = 2.686(4) \text{ cm}/\mu\text{s}$ $q = -3.86(2) \text{ mm}$ $chi^2 = 1.02$
	7	$v_{drift} = 2.399(3) \text{ cm}/\mu\text{s}$ $q = -3.84(2) \text{ mm}$ $\chi^2 = 2.49$		7	$v_{drift} = 2.683(3) \text{ cm}/\mu\text{s}$ $q = -3.90(2) \text{ mm}$ $chi^2 = 0.69$
1250	0	$v_{drift} = 2.806(4) \text{ cm}/\mu\text{s}$ $q = -3.77(2) \text{ mm}$ $chi^2 = 1.31$	1500	0	$v_{drift} = 2.875(4) \text{ cm}/\mu\text{s}$ $q = -3.77(2) \text{ mm}$ $chi^2 = 1.72$
	1	$v_{drift} = 2.806(4) \text{ cm}/\mu\text{s}$ $q = -3.88(2) \text{ mm}$ $chi^2 = 1.50$		1	$v_{drift} = 2.872(4) \text{ cm}/\mu\text{s}$ $q = -3.86(2) \text{ mm}$ $chi^2 = 1.01$
	3	$v_{drift} = 2.806(4) \text{ cm}/\mu\text{s}$ $q = -3.77(2) \text{ mm}$ $chi^2 = 1.56$		3	$v_{drift} = 2.873(4) \text{ cm}/\mu\text{s}$ $q = -3.76(2) \text{ mm}$ $chi^2 = 0.99$
	4	$v_{drift} = 2.800(4) \text{ cm}/\mu\text{s}$ $q = -3.99(2) \text{ mm}$ $chi^2 = 1.45$		4	$v_{drift} = 2.872(4) \text{ cm}/\mu\text{s}$ $q = -4.00(2) \text{ mm}$ $chi^2 = 1.14$
	5	$v_{drift} = 2.799(4) \text{ cm}/\mu\text{s}$ $q = -4.04(2) \text{ mm}$ $chi^2 = 1.45$		5	$v_{drift} = 2.870(4) \text{ cm}/\mu\text{s}$ $q = -4.03(2) \text{ mm}$ $chi^2 = 0.94$
	6	$v_{drift} = 2.807(4) \text{ cm}/\mu\text{s}$ $q = -3.90(2) \text{ mm}$ $chi^2 = 1.21$		6	$v_{drift} = 2.875(4) \text{ cm}/\mu\text{s}$ $q = -3.90(2) \text{ mm}$ $chi^2 = 1.57$
	7	$v_{drift} = 2.803(4) \text{ cm}/\mu\text{s}$ $q = -3.94(2) \text{ mm}$ $chi^2 = 1.04$		7	$v_{drift} = 2.872(4) \text{ cm}/\mu\text{s}$ $q = -3.93(2) \text{ mm}$ $chi^2 = 1.35$

Table A.1. Fit parameters of the plots in Figure 4.15. The fit function is $z = v_{drift}T + q$.

Mixture	Ch	Fit Parameters	Mixture	Ch	Fit Parameters
1	0	$v_{drift} = 2.689(4) \text{ cm}/\mu\text{s}$ $q = -3.74(2) \text{ mm}$ $\chi^2 = 0.89$	2	0	$v_{drift} = 2.897(4) \text{ cm}/\mu\text{s}$ $q = -3.28(2) \text{ mm}$ $\chi^2 = 0.57$
	1	$v_{drift} = 2.685(3) \text{ cm}/\mu\text{s}$ $q = -3.84(2) \text{ mm}$ $\chi^2 = 1.06$		1	$v_{drift} = 2.891(4) \text{ cm}/\mu\text{s}$ $q = -3.41(2) \text{ mm}$ $\chi^2 = 1.28$
	3	$v_{drift} = 2.686(3) \text{ cm}/\mu\text{s}$ $q = -3.73(2) \text{ mm}$ $\chi^2 = 1.09$		3	$v_{drift} = 2.892(4) \text{ cm}/\mu\text{s}$ $q = -3.30(2) \text{ mm}$ $\chi^2 = 1.03$
	4	$v_{drift} = 2.678(4) \text{ cm}/\mu\text{s}$ $q = -3.96(2) \text{ mm}$ $\chi^2 = 1.71$		4	$v_{drift} = 2.879(4) \text{ cm}/\mu\text{s}$ $q = -3.54(2) \text{ mm}$ $\chi^2 = 1.98$
	5	$v_{drift} = 2.676(3) \text{ cm}/\mu\text{s}$ $q = -4.01(2) \text{ mm}$ $\chi^2 = 2.15$		5	$v_{drift} = 2.884(4) \text{ cm}/\mu\text{s}$ $q = -3.61(2) \text{ mm}$ $\chi^2 = 3.21$
	6	$v_{drift} = 2.686(4) \text{ cm}/\mu\text{s}$ $q = -3.86(2) \text{ mm}$ $\chi^2 = 1.02$		6	$v_{drift} = 2.887(4) \text{ cm}/\mu\text{s}$ $q = -3.40(2) \text{ mm}$ $\chi^2 = 0.98$
	7	$v_{drift} = 2.683(3) \text{ cm}/\mu\text{s}$ $q = -3.90(2) \text{ mm}$ $\chi^2 = 0.69$		7	$v_{drift} = 2.889(4) \text{ cm}/\mu\text{s}$ $q = -3.49(2) \text{ mm}$ $\chi^2 = 1.99$
3	0	$v_{drift} = 2.893(4) \text{ cm}/\mu\text{s}$ $q = -3.29(2) \text{ mm}$ $\chi^2 = 0.54$	4	0	$v_{drift} = 2.893(4) \text{ cm}/\mu\text{s}$ $q = -3.30(2) \text{ mm}$ $\chi^2 = 0.69$
	1	$v_{drift} = 2.890(4) \text{ cm}/\mu\text{s}$ $q = -3.42(2) \text{ mm}$ $\chi^2 = 1.13$		1	$v_{drift} = 2.890(4) \text{ cm}/\mu\text{s}$ $q = -3.42(2) \text{ mm}$ $\chi^2 = 2.03$
	3	$v_{drift} = 2.889(4) \text{ cm}/\mu\text{s}$ $q = -3.32(2) \text{ mm}$ $\chi^2 = 1.11$		3	$v_{drift} = 2.888(4) \text{ cm}/\mu\text{s}$ $q = -3.32(2) \text{ mm}$ $\chi^2 = 1.32$
	4	$v_{drift} = 2.879(4) \text{ cm}/\mu\text{s}$ $q = -3.55(2) \text{ mm}$ $\chi^2 = 2.09$		4	$v_{drift} = 2.883(4) \text{ cm}/\mu\text{s}$ $q = -3.55(2) \text{ mm}$ $\chi^2 = 2.29$
	5	$v_{drift} = 2.886(4) \text{ cm}/\mu\text{s}$ $q = -3.63(2) \text{ mm}$ $\chi^2 = 3.67$		5	$v_{drift} = 2.885(4) \text{ cm}/\mu\text{s}$ $q = -3.61(2) \text{ mm}$ $\chi^2 = 3.10$
	6	$v_{drift} = 2.886(4) \text{ cm}/\mu\text{s}$ $q = -3.41(2) \text{ mm}$ $\chi^2 = 0.66$		6	$v_{drift} = 2.888(4) \text{ cm}/\mu\text{s}$ $q = -3.42(2) \text{ mm}$ $\chi^2 = 1.48$
	7	$v_{drift} = 2.890(4) \text{ cm}/\mu\text{s}$ $q = -3.51(2) \text{ mm}$ $\chi^2 = 2.33$		7	$v_{drift} = 2.889(4) \text{ cm}/\mu\text{s}$ $q = -3.50(2) \text{ mm}$ $\chi^2 = 2.42$

Table A.2. Fit parameters of the plots in Figure 4.16. The fit function is $z = v_{drift}T + q$.

E [V/cm]	Ch	Fit Parameters	E [V/cm]	Ch	Fit Parameters
700	0	$\eta = 0.444(19) \text{ cm}^{-1}$ $q = 23.951(19)$ $\chi^2/dof = 0.49$	1000	0	$\eta = 0.280(14) \text{ cm}^{-1}$ $q = 24.198(14)$ $\chi^2/dof = 1.22$
	1	$\eta = 0.454(16) \text{ cm}^{-1}$ $q = 24.808(16)$ $\chi^2/dof = 0.40$		1	$\eta = 0.288(12) \text{ cm}^{-1}$ $q = 25.054(12)$ $\chi^2/dof = 1.18$
	3	$\eta = 0.434(15) \text{ cm}^{-1}$ $q = 24.972(15)$ $\chi^2/dof = 0.29$		3	$\eta = 0.277(12) \text{ cm}^{-1}$ $q = 25.184(12)$ $\chi^2/dof = 1.67$
	4	$\eta = 0.478(23) \text{ cm}^{-1}$ $q = 23.776(20)$ $\chi^2/dof = 2.90$		4	$\eta = 0.310(15) \text{ cm}^{-1}$ $q = 24.084(15)$ $\chi^2/dof = 1.54$
	5	$\eta = 0.520(18) \text{ cm}^{-1}$ $q = 24.700(17)$ $\chi^2/dof = 0.67$		5	$\eta = 0.309(13) \text{ cm}^{-1}$ $q = 24.985(13)$ $\chi^2/dof = 1.30$
	6	$\eta = 0.454(21) \text{ cm}^{-1}$ $q = 23.810(20)$ $\chi^2/dof = 1.76$		6	$\eta = 0.291(15) \text{ cm}^{-1}$ $q = 24.111(15)$ $\chi^2/dof = 1.53$
	7	$\eta = 0.481(17) \text{ cm}^{-1}$ $q = 24.757(17)$ $\chi^2/dof = 0.69$		7	$\eta = 0.292(12) \text{ cm}^{-1}$ $q = 25.031(13)$ $\chi^2/dof = 1.62$
1250	0	$\eta = 0.264(16) \text{ cm}^{-1}$ $q = 24.267(15)$ $\chi^2/dof = 3.35$	1500	0	$\eta = 0.159(16) \text{ cm}^{-1}$ $q = 24.293(17)$ $\chi^2/dof = 1.24$
	1	$\eta = 0.287(15) \text{ cm}^{-1}$ $q = 25.119(14)$ $\chi^2/dof = 3.28$		1	$\eta = 0.176(15) \text{ cm}^{-1}$ $q = 25.133(16)$ $\chi^2/dof = 1.15$
	3	$\eta = 0.271(15) \text{ cm}^{-1}$ $q = 25.243(14)$ $\chi^2/dof = 3.42$		3	$\eta = 0.163(14) \text{ cm}^{-1}$ $q = 25.255(15)$ $\chi^2/dof = 1.81$
	4	$\eta = 0.293(17) \text{ cm}^{-1}$ $q = 24.180(16)$ $\chi^2/dof = 2.72$		4	$\eta = 0.186(17) \text{ cm}^{-1}$ $q = 24.214(17)$ $\chi^2/dof = 1.09$
	5	$\eta = 0.309(15) \text{ cm}^{-1}$ $q = 25.078(14)$ $\chi^2/dof = 3.04$		5	$\eta = 0.196(15) \text{ cm}^{-1}$ $q = 25.104(16)$ $\chi^2/dof = 0.91$
	6	$\eta = 0.280(17) \text{ cm}^{-1}$ $q = 24.201(15)$ $\chi^2/dof = 2.80$		6	$\eta = 0.166(16) \text{ cm}^{-1}$ $q = 24.224(17)$ $\chi^2/dof = 1.16$
	7	$\eta = 0.295(15) \text{ cm}^{-1}$ $q = 25.117(14)$ $\chi^2/dof = 3.16$		7	$\eta = 0.181(15) \text{ cm}^{-1}$ $q = 25.135(15)$ $\chi^2/dof = 1.15$

Table A.3. Fit parameters of the plots in Figure 4.19. The fit function is $\ln(N) = -\eta z + q$.

Mixture	Ch	Fit Parameters	Mixture	Ch	Fit Parameters
1	0	$\eta = 0.013(13) \text{ cm}^{-1}$ $q = 24.501(14)$ $\chi^2/dof = 2.44$	2	0	$\eta = 0.280(14) \text{ cm}^{-1}$ $q = 24.198(14)$ $\chi^2/dof = 1.22$
	1	$\eta = 0.035(12) \text{ cm}^{-1}$ $q = 25.290(13)$ $\chi^2/dof = 2.24$		1	$\eta = 0.288(12) \text{ cm}^{-1}$ $q = 25.054(12)$ $\chi^2/dof = 1.18$
	3	$\eta = 0.017(11) \text{ cm}^{-1}$ $q = 25.439(12)$ $\chi^2/dof = 2.66$		3	$\eta = 0.277(12) \text{ cm}^{-1}$ $q = 25.184(12)$ $\chi^2/dof = 1.67$
	4	$\eta = 0.075(14) \text{ cm}^{-1}$ $q = 24.401(14)$ $\chi^2/dof = 1.31$		4	$\eta = 0.310(15) \text{ cm}^{-1}$ $q = 24.084(15)$ $\chi^2/dof = 1.54$
	5	$\eta = 0.089(13) \text{ cm}^{-1}$ $q = 25.231(13)$ $\chi^2/dof = 1.04$		5	$\eta = 0.309(13) \text{ cm}^{-1}$ $q = 24.985(13)$ $\chi^2/dof = 1.30$
	6	$\eta = 0.043(14) \text{ cm}^{-1}$ $q = 24.412(14)$ $\chi^2/dof = 1.90$		6	$\eta = 0.291(15) \text{ cm}^{-1}$ $q = 24.111(15)$ $\chi^2/dof = 1.53$
	7	$\eta = 0.059(12) \text{ cm}^{-1}$ $q = 25.266(13)$ $\chi^2/dof = 1.70$		7	$\eta = 0.292(12) \text{ cm}^{-1}$ $q = 25.031(13)$ $\chi^2/dof = 1.62$
3	0	$\eta = 0.170(16) \text{ cm}^{-1}$ $q = 24.205(16)$ $\chi^2/dof = 1.97$	4	0	$\eta = 0.140(16) \text{ cm}^{-1}$ $q = 24.134(16)$ $\chi^2/dof = 1.82$
	1	$\eta = 0.187(14) \text{ cm}^{-1}$ $q = 25.045(14)$ $\chi^2/dof = 2.41$		1	$\eta = 0.154(14) \text{ cm}^{-1}$ $q = 24.975(14)$ $\chi^2/dof = 2.35$
	3	$\eta = 0.160(13) \text{ cm}^{-1}$ $q = 25.194(13)$ $\chi^2/dof = 3.06$		3	$\eta = 0.128(13) \text{ cm}^{-1}$ $q = 25.132(13)$ $\chi^2/dof = 3.47$
	4	$\eta = 0.233(17) \text{ cm}^{-1}$ $q = 24.054(17)$ $\chi^2/dof = 1.64$		4	$\eta = 0.216(17) \text{ cm}^{-1}$ $q = 23.975(17)$ $\chi^2/dof = 0.83$
	5	$\eta = 0.242(15) \text{ cm}^{-1}$ $q = 24.952(15)$ $\chi^2/dof = 2.21$		5	$\eta = 0.219(15) \text{ cm}^{-1}$ $q = 24.881(15)$ $\chi^2/dof = 0.46$
	6	$\eta = 0.200(16) \text{ cm}^{-1}$ $q = 24.096(16)$ $\chi^2/dof = 2.29$		6	$\eta = 0.181(16) \text{ cm}^{-1}$ $q = 24.019(16)$ $\chi^2/dof = 0.89$
	7	$\eta = 0.207(15) \text{ cm}^{-1}$ $q = 25.010(15)$ $\chi^2/dof = 2.68$		7	$\eta = 0.182(14) \text{ cm}^{-1}$ $q = 24.936(14)$ $\chi^2/dof = 1.46$

Table A.4. Fit parameters of the plots in Figure 4.20. The fit function is $\ln(N) = -\eta z + q$.

Bibliography

- [1] MEG-II collaboration. “A search for $\mu \rightarrow e\gamma$ with the first dataset of the MEG II experiment”. In: *European Physical Journal C* (2024).
- [2] R. Perrino V. Golovatyuk F. Grancagnolo. “Influence of oxygen and moisture content on electron life time in helium–isobutane gas mixtures”. In: *Nucl. Instr. and Meth. A* (2001).
- [3] MEG II collaboration. “The design of the MEG II experiment”. In: *Eur. Phys. J. C* (2018).
- [4] E. Stevenson and J. Street. “New evidence for the existence of a particle of mass intermediate between the proton and electron”. In: *Physical Review* (1937).
- [5] S. Navas et al. “Particle Data Group”. In: *Physical Review* (2024).
- [6] Y. Fukuda et al. “Evidence for Oscillation of Atmospheric Neutrinos”. In: *Physical Review* (1998).
- [7] SNO Collaboration. “Determination of the e and total 8B solar neutrino fluxes using the Sudbury Neutrino Observatory Phase I data set”. In: *Physical Review* (2007).
- [8] KamLAND Collaboration. “Precision Measurement of Neutrino Oscillation Parameters with KamLAND”. In: *Physical Review* (2008).
- [9] CUORE Collaboration. “New Direct Limit on Neutrinoless Double Beta Decay Half-Life of ^{128}Te with CUORE”. In: *Physical Review* (2022).
- [10] E. P. Hicks and B. Pontecorvo. “Search for Gamma-Radiation in the 2.2-Microsecond Meson Decay Process”. In: *Physical Review* (1948).
- [11] MEG collaboration. “Search for the lepton flavour violating decay $\mu^+ \rightarrow e^+\gamma$ with the full dataset of the MEG experiment”. In: *European Physical Journal C* (2016).

- [12] Y. Kuno and Y. Okada. “Muon decay and physics beyond the standard model”. In: *Rev. Mod. Phys.* (2001).
- [13] SYNDRUM collaboration. “Search for the decay $\mu^+ \rightarrow e^+e^-e^+$ ”. In: *Nuclear Physics* (1988).
- [14] C. M. Perez and L. Vigani. “Searching for the Muon Decay to Three Electrons with the Mu3e Experiment”. In: *Universe* (2021).
- [15] SYNDRUM-II collaboration. “A search for μ - e conversion in muonic gold”. In: *The European Physical Journal C* (2006).
- [16] S. Giovannella. “The detectors of the Mu2e experiment”. In: *JINST* (2020).
- [17] COMET collaboration. “Search for Muon-to-Electron Conversion with the COMET Experiment”. In: *Universe* (2022).
- [18] I. Bigaran et al. “Lepton-flavor-violating tau decays from triality”. In: *Phys. Rev. D* (2023).
- [19] CLEO collaboration. “Search for baryon and lepton number violating decays of the τ lepton”. In: *Phys. Rev. D* (1999).
- [20] BaBar collaboration. “Searches for Lepton Flavor Violation in the Decays $\tau^\pm \rightarrow e^\pm\gamma$ and $\tau^\pm \rightarrow \mu^\pm\gamma$ ”. In: *Phys. Rev. Lett.* (2010).
- [21] LHCb collaboration. “Searches for violation of lepton flavour and baryon number in tau lepton decays at LHCb”. In: *Physics Letter B* (2013).
- [22] S. Banerjee et al. “Snowmass 2021 White Paper: Charged lepton flavor violation in the tau sector”. In: (Mar. 2022). arXiv: 2203.14919 [hep-ph].
- [23] A. M. Baldini et al. “Single-hit resolution measurement with MEG II drift chamber prototypes”. In: *JINST* (2016).
- [24] J.A. Kadyk. “Wire chamber aging”. In: *Nuclear Instruments and Methods in Physics Research A* 300 (1991), pp. 436–479.
- [25] C. Antoine. “Tensions des vapeurs; nouvelle relation entre les tensions et les températures”. In: *Comptes Rendus des Séances de l’Académie des Sciences* (1888).
- [26] G. Cavoto et al. “Operating the GridPix detector with helium-isobutane gas mixtures for a high-precision, low-mass Time Projection Chamber”. In: *JINST* 18.10 (2023), P10035. DOI: 10.1088/1748-0221/18/10/P10035. arXiv: 2305.03599 [physics.ins-det].